

1

2 Sedimentary mechanisms of a modern banded iron formation on
3 Milos Island, Greece

4

5 ^{1,2}Ernest Chi Fru*, ³Stephanos Kiliass, ^{4,5}Magnus Ivarsson, ¹Jayne E. Rattray,
6 ³Katerina Gkika, ²Iain McDonald, ⁶Qian He, ¹Curt Broman

7

8 ¹Department of Geological Sciences, 10691, Stockholm University, Sweden.

9 ²School of Earth and Ocean Sciences, Cardiff University, Park Place, CF10 3AT,
10 Cardiff, UK.

11 ³Department of Economic Geology and Geochemistry, Faculty of Geology and
12 Geoenvironment, National and Kapodistrian University of Athens, Panepistimiopolis,
13 Zographou, 15784, Athens, Greece.

14 ⁴Department of Biology, University of Southern Denmark, Campusvej 55, Odense M,
15 DK5230, Denmark

16 ⁵Department of Palaeobiology, Swedish Museum of Natural History, Box 50007,
17 Stockholm, Sweden.

18 ⁶School of Chemistry, Cardiff University, Park Place, CF10 3AT, Cardiff, UK.

19

20 *Corresponding author

21 Tel: +44(0) 29 208 70058

22 Email: ChiFruE@cardiff.ac.uk

23

24 Short title: A modern banded iron formation

Abstract. An Early Quaternary shallow submarine hydrothermal iron formation (IF) in the Cape Vani sedimentary basin (CVSB) on Milos Island, Greece, displays banded rhythmicity similar to Precambrian banded iron formation (BIF). Sedimentary and stratigraphic reconstruction, coupled to biogeochemical analysis and micro-nanoscale mineralogical characterization, confirm the Milos IF as a modern BIF analogue. Spatial coverage of the BIF-type rocks in relation to the economic grade Mn ore that brought prominence to the CVSB implicates tectonic activity and changing redox in their deposition. Field-wide stratigraphic and biogeochemical reconstruction demonstrate two temporal and spatially isolated iron deposits in the CVSB with distinct sedimentological character. Petrographic screening suggests the previously described photoferrotrophic-like microfossil-rich IF (MFIF), accumulated on basement andesite in a ~150 m wide basin, in the SW margin of the basin. A strongly banded non-fossiliferous IF (NFIF) sits on top the Mn-rich sandstones at the transition to the renowned Mn-rich formation, capping the NFIF unit. Geochemical evidence relates the origin of the NFIF to periodic submarine volcanism and water column oxidation of released Fe(II) in conditions apparently predominated by anoxia, similar to the MFIF. Raman spectroscopy pairs hematite-rich grains in the NFIF with relics of a carbonaceous material carrying an average $\delta^{13}\text{C}_{\text{org}}$ signature of ~-25‰. However, a similar $\delta^{13}\text{C}_{\text{org}}$ signature in the MFIF is not directly coupled to hematite by mineralogy. The NFIF, which post dates large-scale Mn deposition in the CVSB, is composed primarily of amorphous Si (opal- $\text{SiO}_2 \cdot n\text{H}_2\text{O}$) while crystalline quartz (SiO_2) predominates the MFIF. An intricate interaction between tectonic processes, changing redox, biological activity and abiotic Si precipitation are proposed to have collectively formed the unmetamorphosed BIF-type deposits in a shallow submarine volcanic center.

Keywords: Banded iron formation; BIF analogue; Hydrothermal activity; Iron cycling; Silica cycling.

1 Introduction

Banded iron formations (BIFs), are marine sedimentary deposits containing at least 15% Fe, marked by Fe-rich bands alternating with Si-rich layers that formed predominantly during the Precambrian (James, 1954; Gross, 1980; Simonson, 1985, 2003; Bekker et al., 2010). Recently, an Early Quaternary iron formation (IF), ~2.0 million years old, displaying banded rhythmicity typical of Precambrian banded iron formations (BIF) was serendipitously discovered in the Cape Vani sedimentary basin (CVSB) on Milos Island, Greece (Chi Fru et al., 2013, 2015). Before this discovery, Cape Vani was long known to host Mn oxide ores of economic potential (Hein et al., 2000; Liakopoulos et al., 2001; Glasby et al., 2005; Kiliass et al., 2007). Milos is an emergent volcano on the Hellenic Volcanic Arc (HVA) where arc-volcanism and seafloor hydrothermal activity occur in thinned pre-Alpine to Quaternary continental crust (Kiliass et al., 2013b) (Fig. 1). The first reported IF from Cape Vani is unmetamorphosed and contains diverse microfossils encrusted by hematite, with ferrihydrite proposed as a primary precursor mineral (Chi Fru et al., 2013, 2015). Field stratigraphy, rare earth elements (REEs), stable isotopes, petrographic and microfossil studies point to microbial Fe deposition in a semi-enclosed, shallow submarine basin under conditions analogous to those that formed the Precambrian Algoma-type BIFs near volcanic centers (Chi Fru et al., 2015). These earlier reports assumed a one-time basin-wide depositional event and a common origin for all Fe-rich sedimentary rocks in the CVSB.

However, it remains unclear what sedimentary processes caused the distinct deposition of the BIF-type rocks in a basin where Mn precipitation was apparently widespread at various intervals. Moreover, it is not known how the Mn ores relate temporally and spatially to Fe deposition in the ~1 km long CVSB. This knowledge

may provide clues to processes that triggered large-scale deposition of similar Proterozoic Fe-Mn-rich deposits (Roy, 2006; Tsikos et al., 2010; Beukes et al., 2016). Here, new sedimentological, petrological and biogeochemical evidence describes cycles of periodic precipitation of shallow submarine Si and Fe-rich sedimentary rocks and the plausible mechanisms that enabled their temporal and spatial separation from the Mn deposits in the CVSB. The data reveal a much more complex depositional system not only controlled by microbial Fe(II) oxidation as previously proposed (Chi Fru et al., 2013, 2015), but illuminates episodic submarine hydrothermal activity coupled to changing redox conditions as a central mechanism in the formation of the banded iron rocks.

1.1 Geological setting

K-Ar radiometric dating of biotite and amphiboles belonging to the dacitic/andesitic lava domes flooring the CVSB basin gave an Upper Pliocene age of 2.38 ± 0.1 Ma (Fytikas et al., 1986; Stewart and McPhie, 2006). The fossiliferous sandstones/sandy tuffs hosting the Mn-rich deposit, which contain the gastropod mollusk guide fossil, *Haustator biplicatus* sp. (Bronn, 1831), indicate an Upper Pliocene-Lower Pleistocene age. The geology, Fe and Mn mineralization of the CVSB have previously been described in detail (Plimer, 2000; Hein et al., 2000; Liakopoulos et al., 2001; Skarpelis and Koutles, 2004; Glasby et al., 2005; Stewart and McPhie, 2006; Kiliyas, 2011; Alfieris and Voudouris, 2005; Alfieris, 2006; Alfieris et al., 2013; Chi Fru et al., 2013, 2015; Papavassiliou et al., 2017). Briefly, the Milos IF is part of the CVSB, a recently emergent sedimentary rift basin located NW of Milos Island, along the HVA in the Aegean Sea, Greece (Fig. 1). It hosts a fossil analogue of active shallow-submarine hydrothermal activity on the coast of Milos Island (Dando et al., 1995).

The CVSB developed within a shallow-submarine rhyolitic-dacitic volcanic center, filled up mainly by a ~35-50 m thick stratigraphic succession of volcanoclastic/epiclastic sandstones and sandy tuffs spanning Upper Pliocene to Lower Pleistocene, 35-40% of which is hydrothermally mineralized by Mn oxides and barite (Hein et al., 2000; Liakopoulos et al., 2001; Skarpelis and Koutles, 2004; Papavassiliou et al., 2017). Sedimentologic and ichnologic data, including sedimentary structures, lamellibranch, echinoid and brachiopod fossils, the gastropod mollusk fossil, *Haustator biplicatus* (Bronn, 1831), and microbially induced sedimentary structures (e.g., Kiliyas, 2011), suggest that most of the CVSB sandstones/sandy tuffs hosting the Mn-rich deposit, are foreshore to shoreface shallow submarine deposits, formed at a maximum depth of 200 mbsl. Over the last 0.8 Myr, fluctuating water depths due to sea-level change of up to 120 m and volcanic edifice building, has resulted in tectonic uplift of ~250 m (Papanikolaou et al., 1990). The CVSB infill, currently 35 m above sea level, is tectonically bound by extrusive rhyolite to the north, framed by elevated andesitic-dacitic centres, with the Cape Vani and the Katsimoutis dacitic lava domes being the most prominent (Fig. 1).

2 Methodology

2.1 Sample preparation

Prior to mineralogical and geochemical analysis, exposed rock surface layers were sawn and removed. GeoTech Labs (Vancouver, Canada) produced doubly polished thin sections for mineralogical and textural analysis. Trace and rare earth elements analysis was performed on pulverized powders digested with a mixture of HNO₃, HF and heat until a clear solution was obtained (Chi Fru et al., 2013, 2015).

2.2 Mineralogical analysis

2.2.1 X-Ray Diffraction (XRD) analysis

A PANalytical Xpert-pro diffractometer at room temperature, 45 kV, 40 mA and 1.5406 Å wavelength and Cu-K α radiation and Ni-filter, was used for Powder X-Ray Diffraction (PXRD) analysis. Samples were analyzed between 5-80° in step sizes of 0.017° with continuous mode scanning step time of 50.1650 s while rotating.

2.2.2 Raman spectroscopy

Raman analysis was performed with a confocal laser Raman spectrometer (Horiba instrument LabRAM HR 800), equipped with a multichannel air-cooled (-70°C) 1024 x 256 pixel charge-coupled device (CCD) array detector as previously described (Chi Fru et al. 2013, 2015). Spectral resolution was ~0.3 cm⁻¹/pixel. Accuracy was determined by a repeated silicon wafer calibration standard at a characteristic Raman line of 520.7 cm⁻¹.

2.2.3 Transmission electron microscopy

Specimens for transmission electron microscopy (TEM) were prepared from the crushed rock specimen powder. This was followed by dry-dispersal onto a 300 mesh holey carbon TEM Cu grid. Microscopy was conducted using a JEOL 2100 TEM with a LaB₆ source in the School of Chemistry, Cardiff University, operated at 200kV. The X-EDS analysis was performed with an Oxford Instrument SDD detector X-Max^N 80 T.

2.2.4 Scanning electron microscopy

Scanning Electron Microscopy-Energy Dispersive Spectroscopy (SEM-EDS) analysis was done on a FEI QUANTA FEG 650 ESEM. Images were captured at 5 kV and EDS data collected at 20 kV, using an Oxford T-Max 80 detector (Oxford Instruments, UK). The analyses were performed in low vacuum to minimize surface charging of uncoated samples. EDS elemental maps were collected for 30 min or until the signal had stabilized, indicated by a clear distribution trend. The data were further processed with the Oxford Aztec software.

2.3 Geochemical analysis

2.3.1 Laser ablation ICP-MS and trace element analysis

Laser Ablation-Inductively Coupled Plasma-Mass Spectrometry (LA-ICP-MS) was performed at Cardiff University on polished thin sections. The LA-ICP-MS system comprised a New Wave Research UP213 laser system coupled to a Thermo X Series 2 ICP-MS. The laser was operated using a frequency of 10 Hz at pulse energy of ~5mJ for an 80µm diameter beam using lines drawn perpendicular to the layering and at a movement speed of 26 microns sec⁻¹. Samples were analyzed in time resolved analysis (TRA) mode using acquisition times of between 110 and 250 seconds; comprising a 20 second gas blank, 80-220 second ablation and 10 second washout. Dwell times varied from 2 msec for major elements to 35 msec for low abundance trace elements. Blank subtraction was carried out using the Thermo Plasmalab software before time resolved data were exported to Excel.

Separated and independently pulverized banded layers were digested by lithium borate fusion followed by major, trace and rare earth element (REE) analyses using ICP- Atomic Emission Spectrometry-Mass Spectrometry (ICP-AES-MS) and X-Ray Florescence (XRF) at Bureau Veritas (Ankara). Geochemical data were compared

with previously published results for the more widely investigated Mn deposits (Hein et al., 2000; Liakopoulos et al., 2001; Glasby et al., 2005).

2.3.2 Isotope analysis

C, N and S isotopic composition for the pulverized samples was determined as previously described (Chi Fru et al., 2013, 2015), following combustion in a Carlo Erba NC2500 analyzer and analyzed in a Finnigan MAT Delta V mass spectrometer, via a split interface to reduce gas volume. Reproducibility was calculated to be better than 0.15‰ for $\delta^{13}\text{C}$ and $\delta^{15}\text{N}$ and 0.2‰ for $\delta^{34}\text{S}$. Total C and N concentrations were determined simultaneously when measuring the isotope ratios. The relative error was <1% for both measurements. For carbon isotopic composition of organic carbon, samples were pre-treated with concentrated HNO_3 prior to analysis.

2.4 Organic geochemistry analysis

Lipid biomarker and compound specific $\delta^{13}\text{C}$ analyses were executed on powdered samples of sectioned bands from which exposed surface layers had been removed. Modern sediments from Spathi Bay, 36°40'N, 24°31'E, southeast of Milos Island, collected by push coring at 12.5 m below the seafloor were freeze-dried prior to extraction to aid the identification of potential syngenetic biomarkers in the Quaternary rocks. Between 4-6 g of ground samples were ultrasonically extracted using 3×Methanol, 3×(1:1) Methanol:Dichloromethane (DCM), and 3×DCM and extracts were combined and dried under N_2 . Samples were subsequently re-dissolved in DCM then methylated following the method of Ichihara and Fukubayashi (2010). The resulting residue was silylated using, 20 μl pyridine and 20 μl (N, O-Bis(trimethylsilyl)trifluoroacetamide) BSTFA and heated at 60°C for 15 min. Total

lipid extracts were analyzed using a Shimadzu QP 2010 Ultra gas chromatography mass spectrometer (GC/MS). Separation was performed on a Zebron ZB-5HT column (30 m x 0.25 mm x 0.10 μ m) with a helium carrier gas flow at 1.5 ml min⁻¹. Samples were injected splitless, onto the column at 40°C with the subsequent oven temperature program ramped to 180°C at a rate of 15°C min⁻¹, followed by ramping to 325°C at a rate of 4°C min⁻¹ and a final hold for 15 min. The MS was set to scan from 50 to 800 m/z with an event time of 0.70 sec and a scan speed of 1111 u/sec. All peaks were background subtracted and identification confirmed using the NIST GC/MS library and literature spectra. Contamination was not introduced into the samples, as blank samples worked up concurrently with the rock fractions had results comparable to the ethyl acetate instrument blank.

2.5 Chemical weathering analysis

Chemical index of alternation (CIA) was used to determine whether variations in chemical weathering intensities would in addition to hydrothermal activity deliver materials into the depositional basin from the continent, according to the formula: $CIA = Al_2O_3 / (Al_2O_3 + CaO + Na_2O + K_2O) \times 100$. Extensively applied, the CIA index reveals subtle changes in weathering fluxes (Nesbit and Young, 1982; Maynard, 1993; Bahlburg & Dobrzinski, 2011), where increasing CIA values generally indicate amplified chemical dissolution of rocks and selective release of dissolvable CaO, Na₂O and K₂O into solution (Nesbit & Young, 1982; Maynard, 1993; Bahlburg & Dobrzinski, 2011). The broken rock particles enriched in the poorly soluble Al₂O₃ fraction, settle to the seafloor as weathered sediments carrying a chemical composition different from the source. In the absence of chemical dissolution, no net chemical change is expected in the composition of sediments

compared to source and thus a low CIA index. CIA indices for detritus of 0-55, 55-75 and >75, are considered unweathered, unweathered to slightly weathered and weathered to highly weathered, respectively (Nesbit & Young, 1982; Maynard, 1993; Bahlburg & Dobrzinski, 2011).

2.6 Redox analysis

Redox depositional conditions were evaluated using the sequential Fe extraction redox proxy (Poulton and Canfield, 2005, 2011), combined with REE composition of the sediment (Planavsky et al., 2010).

2.6.1 REE redox analysis

REE data obtained as described in section 2.3.1 were normalized with the North American Shale Composite (NASC) to maintain consistency with previous studies in which NASC-normalized REE data (SN) were reported for the Milos BIF-type rocks (Chi Fru et al., 2013, 2015). The data were further normalized with the Post Archean Australian Shale (PAAS) (McLennan, 1989) standard for comparative purposes, according to Bau and Dulski (1996). Ce anomalies, calculated from Ce/Ce^* ($Ce_{(SN)}/0.5Pr_{(SN)} + 0.5La_{(SN)}$) and Pr/Pr^* ($Pr_{(SN)}/0.5Ce_{(SN)} + 0.5Nd_{(SN)}$) values, were considered significant when Ce/Ce^* and Pr/Pr^* were less than and greater than 1, respectively (Bau and Dulski et al., 1996; Planavsky et al., 2010).

2.6.2 Sequential iron extraction redox analysis

This analysis was performed on three representative MFIF samples and the six sectioned bands of a typical NFIF sample using the method developed by Poulton and Canfield (2005) and data interpreted accordingly (e.g., Canfield and Poulton, 2005,

2011; Guilbaud et al. 2015; Sperling et al. 2015). Reagent blanks and geological standards were used for data calibration.

3 Results

3.1 Lithostratigraphy

Sedimentary structures, grain-size trends, lateral facies variations, vertical stacking trends, and key stratigraphic surfaces form the basis for facies analysis. Field-wide sedimentological and lithostratigraphical mapping of the CVSB in the summer and fall of 2014 enabled the assessment of the lateral and vertical coverage of the Milos iron oxide-rich facies relative to the Mn-rich sandstones that dominate the Early Quaternary sedimentary basin (Fig. 2). Six stratigraphic sections, representing marine siliciclastic lithofacies sequences, were investigated along a ~1 km SW-NE trending portion of the CVSB infill (Supplementary Figs 1-7). Sequence stratigraphy was conducted on outcrops and vertical shafts and tunnels left behind by previous Mn mining activity. Two of those sections; Section A located at 36°44'17.85''N, 24°21'17.72''E and Section B located at 36°44'35.11''N, 24°21'11.25''E, contain stratigraphic units composed of layered, bedded, or laminated rocks that contain ≥ 15 % Fe, in which the Fe minerals are commonly interlayered with quartz or chert, in agreement with the definition of Precambrian BIFs (James, 1954; Gross, 1980; Bekker et al., 2010). These IFs are descriptively referred to here as microfossiliferous iron formation (MFIF) according to Chi Fru et al. (2013, 2015), and non-microfossiliferous iron formation (NFIF) (this study), respectively (Fig. 2). The MFIF and the NFIF occupy at most ~20% of the entire CVSB infill. The stratigraphy and sedimentary lithofacies are illustrated below, using lithofacies codes modified after

Bouma (1962), Miall (1978, 1985), Lowe (1982), Mutti (1992) and Shanmugam (2016).

Further field stratigraphic survey revealed considerable lithologic variability within three fault-bounded volcanosedimentary sub-basins in the CVSB (Fig. 2), which for the sake of simplicity are referred to as Basin 1—host of the MFIF; Basin 2—host of economic grade Mn ore; and Basin 3—host of the NFIF (Fig. 2). Each section is framed by distinct marginal normal faults that strike in the NW-SE and NE-SW to NNE-SSW directions, distinguishable by distinct lateral sedimentary facies exhibiting unique vertical sequence stratigraphy (Fig. 2; Supplementary Figs 1-7). Faulting in the CVSB is related to major geographical activation of extensional structures at intervals that shaped Milos into a complex mosaic of neotectonic units (Papanikolaou et al., 1990; van Hinsbergen et al., 2004).

3.1.1 Section A (36°44'17.85''N, 24°21'17.72''E)

Informally known as “Little Vani”, Section A is the type section containing the MFIF at the base. It crops out in the W-SW edge of the CVSB (Figs 1 & 2) as a ~6-7 m high cliff resting stratigraphically on submarine dacitic and andesitic lavas and domes. This section extends laterally in the N-NE direction for an estimated 300–500 m.

Lithologically, the MFIF comprises laminated and massive fine-grained red and white weathered ferruginous jaspelitic red chert layers (Chi Fru et al., 2013, 2015). The chert layers contain morphologically distinct Fe minerals dispersed in a fine-grained siliceous matrix (Fig. 3), marked by the notable absence of pyrite and an extremely low S content (Chi Fru et al., 2013, 2015). Layers are tabular and typically laterally continuous at scales of several meters, whereas wave and current structures (e.g., cross-lamination) are generally absent from the MFIF. The hematite-rich MFIF

laminae (Table 1) are built by massive encrustation of anoxygenic photoferrotrophic-like microbial biofilms by precipitated Fe (Chi Fru et al., 2013). The base of the MFIF outcrop, is visibly mineralized by black diffused bands/veins composed of Mn oxides (Fig. 4 & Table 1).

A markedly ferruginous 2-3 m-thick section immediately overlies the MFIF, comprising a distinct package of Fe-rich beds that transition up the section (Figs 4A & 5). The lower 1-2 m consist of fine-grained sandstone beds that are well to moderately sorted, containing a 20-40 cm thick portion dominated by plane parallel-laminated sandstone/sandy tuff, massive to plane parallel-laminated sandstone/sandy tuff, and massive sandstone/sandy tuff lithofacies (Fig. 5; Supplementary Fig. 1). The fabric of these Fe-rich sandstone facies consists of sub-angular to sub-rounded and 100–600 μm fine to medium-grained volcanoclastic K-feldspar grains, making up to 75% of the total rock, with variable amounts of quartz and clay mineral grains.

The latter are overlain by a ~1-1.5 m sequence of poorly-sorted tabular clast-supported pebble-to-cobble conglomerate beds with an erosional base, grading upward into coarse to medium-grained sandstone/sandy tuff beds, with alternating conglomerate cycles (Fig. 5), averaging 20-40 cm in thickness. The cobble/pebble conglomerate clasts include intraformational volcanic rocks (dacite, andesite), allochthonous volcanoclastic sandstone, and volcanoclastic microclasts (e.g. K-feldspar), cemented by hematite (Fig. 5; Chi Fru et al., 2013; Kilias et al., 2013a). Towards the westernmost edge of the “Little Vani” section, there is a facies change from the graded pebbly conglomerate/sandy tuff rhythms to a predominantly Fe-rich conglomerate bed (Fig. 6A), termed the conglomerate-hosted IF (CIF) in Chi Fru et al. (2015), with a maximum thickness of ~0.5 m and a cobble size range of ~10 cm. The Fe-rich conglomerate bed transitions upward into medium-grained pebbly reddish

ferruginous sandstones with thin volcanic rock and sandstone pebble lenses. This, in turn, grades upwards into a very-fine-grained greenish glauconite-bearing plane parallel-laminated sandstone to siltstone bed; characterized by soft-sediment deformation structures, such as flame structures, convolute bedding and lamination structures, loop bedding, load casts, and pseudonodules (Supplementary Figs 1-2).

The “Little Vani” section is eventually capped along an erosional surface by an overlying 1-2 m thick section dominated by medium to fine-grained and moderately to poorly-sorted reddish Fe-rich tabular sandstone beds, 10–40 cm thick, topped by patchy sub-cm to cm-thick Mn-rich sandstones (Fig. 5; Supplementary Figs 1-2). Dominant lithofacies of the Fe-rich sandstone cap include planar and hummocky cross-bedding, exhibiting bioturbation in places. The Fe-rich lithofacies cap is laterally discontinuous, thinning out basinwards towards the N-NE, and can be observed smoothly grading into a 1-2 m thick section composed of cm to sub-cm-thick Mn-rich volcanoclastic sandstone lithofacies, described below in Section B. No Fe-rich hydrothermal feeder veins are obvious in the MFIF. However, feeder veins and Mn horizons can be observed to truncate laminations in the MFIF, and up through the whole “Little Vani” section (e.g., Figs 4C & 5).

The MFIF rests directly on the submarine dacites-andesites that were deposited in a relatively shallow submarine environment (Stewart and McPhie, 2006). The fine-grained, finely laminated nature of the MFIF, and, the lack of evidence of current or wave structures (e.g., symmetric ripples or hummocky cross-stratification), coupled to the absence of volcanogenic detrital particles and intraclast breccia structures, indicate a low energy sedimentation environment, marked by negligible volcanic interference (e.g., Tice and Lowe, 2006; Konhauser et al., 2017). This interpretation is supported by the observed enrichment of Fe in the MFIF; a

characteristic of relatively deeper water lithofacies (Konhauser et al., 2017). This view is compatible with the proposition that hematite enrichment in the MFIF was under the control of photoferrotrophic biofilms (Chi Fru et al., 2013) known to thrive at lower light intensities (Kappler et al., 2005; Li et al., 2013; Konhauser et al., 2017). The quiet environmental conditions would have ensured the formation of such stable photoferrotrophic biofilms over extended periods of time that would have facilitated the oxidation of hydrothermally released Fe(II) and the deposition of Fe(III) minerals.

In the overlying sandstone-conglomerate facies, the presence of sedimentary structures indicative of wave action and currents (e.g. cross-stratification), that signify rapid deposition during a high energy event, are consistent with a switch to a shallow-submarine high energy environment (Stewart and McPhie, 2006; Chi Fru et al., 2015). This shift in depositional environments may have been controlled by a combination of submarine volcano-constructional processes, synvolcanic rifting and volcano-tectonic uplift known to have formed the CVSB (Papanikolaou et al., 1990; Stewart and McPhie, 2006).

3.2 Section B (36°44'35.11"N, 24°21'11.25"E)

This ~8-10 m thick fault-bounded stratigraphic section, here referred to as "Magnus Hill", is the type section that contains the NFIF (Figs 2 & 7; Supplementary Figs 3-4). Two lithostratigraphic units—a lower unit A and an upper unit B—are identified in this study. Unit A is made up of a lower sandstone facies that is ~4-5 m thick, dominated by a Mn-oxide cement, overlain by reddish brown Fe-rich massive sandstone beds (Fig. 8 & Supplementary Figs 3-4). The lower sandstone facies represents the host of the main economic grade Mn oxide ores in the CVSB. This constitutes part of a separate study devoted to the Mn ores and will not be dealt with

further here. Unit B, ~5 m thick, unconformably overlies unit A and comprises two distinct packages of beds that transition up section from brownish pebble conglomerate layers (0.5-1.0 m thick), in contact with the very fine-grained NFIF deposit (Supplementary Fig. 8 & 9). The NFIF is capped by patchy cm-thick crustiform Mn oxides. Bifurcating feeder veins composed of barite, quartz and Mn-Fe-oxide minerals cut through the underlying sandstone beds (Supplementary Fig. 4).

The NFIF is composed of strongly banded Fe-rich rocks (Fig. 7) exposed on the topmost part of “Magnus Hill”. About 2-3 m thick, the NFIF consists of mm to sub-mm thick, dark grey and brown Fe-rich bands, interbanded with reddish brown Si-rich layers (Figs 7 & 9-11; Supplementary Figs 10-11). Sedimentary structures in the NFIF are predominantly characterized by rhythmic mm to sub-mm thick laminations (e.g., Fig. 7). The iron oxide-rich bands made up mainly of hematite (Table 1 & Fig. 10C) are typically composed of very fine-grained angular to sub-angular volcanic dust material (i.e., fine volcanic ash with particle size under 0.063 mm, K-feldspar, tridymite and cristobalite (Table 1) in an amorphous Si and crystalline hematite matrix (Fig. 12)). The predominantly amorphous Si-rich bands are typically planar, finely laminated and composed of microcrystalline to cryptocrystalline ferruginous chert.

The NFIF is directly overlain by a ~1 m thick laminated to massive well-indurated, nodular-pisolitic ironstone bed (Fig. 8A, C & D) that locally preserves a sub-horizontal fabric reflecting the bedding in the original sediment or contain various ferruginous clasts such as fragments, nodules, pisoliths, and ooliths set in a hematite-rich siliceous matrix (Fig. 8C). Scattered cm scale pisoliths display a crude concentric internal layering, characterized by open and vermiform voids filled by cauliflower-like Mn oxides overprint (Fig. 8D). The ferruginous NFIF lithofacies are interpreted

to represent the deepest water deposits in the “Magnus Hill” section based on its very fine-grained sedimentary composition, fine laminations and a paucity of intraclast breccias. These, combined with the lack of evidence for wave and current-formed sedimentary structures (e.g., hummocky cross-stratification, trough, ripple cross-stratification, and erosional contacts), indicate quiet water low energy sedimentation, likely below wave base (Simonson and Hassler, 1996; Trendall, 2002; Krapež et al., 2003; Konhauser et al., 2017).

We interpret that each graded Fe oxide-rich band of the NFIF (Supplementary Fig. 9), represents an individual fallout deposit from a proximal pyroclastic eruption. This interpretation is supported by normal grading in fine volcanic ash content that reflects their likely origin as pyroclastic fallout deposits in an otherwise quiet water setting. For example, tridymite is a stable SiO_2 polymorph formed at low pressures of up to 0.4 GPa and at temperatures of $\sim 870\text{--}1470^\circ\text{C}$ (Swamy et al., 1994; Morris et al., 2016). The coincidence of tridymite formation with silicic volcanism is in agreement with the widespread distribution of andesite, dacite and rhyolite lava domes in the CVSB. For example, vapour phase production of tridymite together with sanidine identified in this study (Fig. 10) and Fe oxides is principally associated with rhyolite ash flow (Breitkreuz, 2013; Galan et al., 2013). Similarly, Cristobalite is a SiO_2 polymorph associated with high temperature rhyolitic eruptions (Horwell et al., 2010). Finally, in situ carbonaceous laminations are absent, suggesting that benthic microbial mat growth had no influence on deposition of the NFIF. Ironstones overlying the NFIF are difficult to interpret with the existing data, but may represent supergene ferruginous duricrust formation resulting from subaerial weathering (Anand et al., 2002).

3.3 Geochemistry

3.3.1 Geochemistry of the individual Fe-rich and Si-rich bands

The SEM-EDS-electron micrographs of the NFIF thin sections reveal distinct Fe bands and Si-rich layers alternating periodically with each other in a fine sediment matrix as shown by the grain size (Figs 9 & 11 & Supplementary Figs 9-11). Laser ablation ICP-MS line analysis indicates Si and Fe count intensities in the Milos BIF-type rocks are comparable to the 2.5 Ga Precambrian BIF reference from the Kuruman IF formation, Transvaal Supergroup, South Africa (Fig. 11). The laser ablation ICP-MS data further show an inverse correlation between Fe and Si, the two major elemental components of BIFs, irrespective of the thousands of millions of years gap separating the Precambrian deposit from the recently formed Milos IF formation.

3.3.2 Mineralogy of the individual Fe-rich and Si-rich bands

No other Fe(III)(oxyhydr)oxide minerals have been identified in the Cape Vani Fe-rich facies different from hematite. Electron imaging of the NFIF Fe-rich bands suggests Si, Al and K-rich phases are mostly associated with the volcanoclastic material predominated by K-feldspar clasts (Fig. 9; Supplementary Figs 10 & 11). A unique feature of the NFIF is that the hematite in the Fe-rich bands occurs in tight association with a carbonaceous material (Fig. 10C), but not for the hematite in the Fe-rich sandstones and in the MFIF. This is also the case for the CIF overlying the MFIF. Hematite showing a fluffy texture and at times presenting as framboidal particles, is sprinkled in the Si-rich cement containing traces of Al and K in the MFIF rocks (Fig. 3). Lack of association of the framboidal-iron-rich particles with S, following SEM-EDS analysis, rules out a pyrite affiliation and is consistent with the

non-sulfidic depositional model suggested by the sequential iron extraction redox proxy (Fig. 13D). TEM analysis suggests platy nano-Fe oxide-rich particles predominate in the NFIF and MFIF, confirmed by overlaid X-ray Energy Dispersive spectra taken from selected areas (Fig. 12) and consistent with the XRD data showing hematite in both samples. The platy hematite needles in the Milos BIF-type rocks are morphologically, and by size, comparable to hematite needles reported in the ~2.5 Ga Kuruman BIFs (Sun et al., 2015).

Unlike the Fe-rich bands, volcanoclasts in the Si-rich bands are much smaller in size, occurring mainly as fine-grained (Supplementary Fig. 8-11), signifying predominant precipitation during periods of weakened hydrothermal activity. The SiO₂ matrix in both the MFIF and NFIF are fine-grained, occurring mainly as amorphous opal in the NFIF (Figs 10B & 12A-B), whereas in the MFIF it is mainly present as crystalline quartz (Fig. 12C-D). Relative concentrations of Al, K and Ti in the samples are generally low, with bulk-measured concentrations in both the Si-/Fe-rich bands, together with the SiO₂ and Fe₂O₃ content, strongly covarying with continental crust concentrations (Fig. 13A). Mn impregnation of the MFIF, preserved in the form of replacement layers mostly identified as cryptomelane [K(Mn⁴⁺, Mn²⁺)₈O₁₆] (Table 1), is below detection in the NFIF. Rare hausmannite (Mn²⁺Mn³⁺₂O₄) was detected in a few cases in the MFIF (Fig. 10D).

3.3.3 Hydrothermal versus continental weathering

Trends of major elements from which CIA indices were calculated (Fig. 13B), covary with those of the continental crust (Fig. 13A). Continental crust averages, refer to the zone from the upper continental crust to the boundary with the mantle (Rudnick & Gao, 2003). The calculated CIA indices average 52 with one outlier at 22 (Fig. 13B).

No distinct relationship could be established between the CIA indices and the respective IFs or between the distinct alternating Si- and Fe-rich bands (Fig. 13). Highly weathered clay minerals resulting from the chemical decomposition of volcanic rocks, e.g., kaolinite representing maximum CIA values of 100 or 75-90 for illite, are absent in the analyzed materials. The absence of carbonates in the rocks strengthened the CIA indices, since CIA indices are expected to be lower when Ca carbonates are present (Bahlburg and Dobrzinski, 2011). TiO_2 content, a detrital proxy, is mostly constant and covaries with the CIA values (Fig. 13B), suggesting little variability and limited continental weathering input. A fairly strong negative linear correlation was found between SiO_2 and Fe_2O_3 values normalized to TiO_2 (inset, Fig. 13B).

3.3.4 Redox reconstruction

Redox reconstruction by sequential iron extraction (Poulton and Canfield, 2005, 2011; Guilbaud et al., 2015; Sperling et al., 2015) is consistent with deposition of both the MFIF and NFIF facies beneath an anoxic, ferruginous bottom water body (Fig. 13C-D). The shale-normalized REE values ($\text{REE}_{(\text{SN})}$) for both the MFIF and NFIF are consistent with previous reports (Chi Fru et al., 2013, 2015), showing patterns typical of marine sedimentary environments affected by hydrothermal activity throughout Earth's history (e.g., Planavsky et al., 2010). There is a notable absence of significant negative $\text{Ce}_{(\text{SN})}$ anomalies for both the MFIF and NFIF (Fig. 14A-B). These observations are statistically corroborated by true Ce anomalies. Further, the Eu/Eu^* anomaly averages for the MFIF and NFIF and the distinct Fe-/Si-rich bands, suggest a $\sim 2\times$ higher Eu/Eu^* signal for the Si-rich bands relative to the Fe-rich bands and between the MFIF and NFIF deposits (Fig. 14C). Average Pr and

Yb shale-normalized ratios (Pr/Yb*), a light vs. heavy REE enrichment proxy (Planavsky et al., 2010), indicate similar depleted levels of light and heavy REE in both the NFIF and MFIF, as well as in the Fe- and Si-rich bands (Fig. 14C). This independent verification of the anoxic depositional conditions using the sequential Fe proxy, suggests the NASC normalization protocol effectively captures the redox depositional conditions of the Milos IF.

3.4 Lipid biomarker distribution and chemotaxonomy

Bulk $\delta^{13}\text{C}_{\text{org}}$ averaged -25.4‰ (SD: ± 0.22); -25.2‰ (± 0.26) for NFIF Fe-/Si-rich bands and -25.6‰ (SD: ± 0.12) for bulk MFIF, respectively (Table 2). A fractionation effect between the alternating Fe-/Si-rich layers ($\Delta^{13}\text{C}_{\text{Fe-rich NFIF-Si-rich NFIF}}$) is estimated to be $\sim 0.23\text{‰}$ (SD: ± 0.036), while $\Delta^{13}\text{C}_{\text{Fe-rich NFIF-MFIF}}$ and $\Delta^{13}\text{C}_{\text{Si-rich NFIF-bulk MFIF}}$ is 0.13‰ (SD: ± 0.11) and 0.36‰ (SD: ± 0.14), respectively. These differences are small and within the margin of error of analysis, suggesting no strong distinction in $\delta^{13}\text{C}_{\text{org}}$ preserved in the different IFs and their various facies. They are interpreted to mean similar carbon fixation processes operated during intervals of predominant Si and Fe(III)(oxyhydr)oxides deposition in both IFs. Attempts to discriminate between these environments by lipid biomarker analysis revealed mainly $\text{C}_{16}\text{-C}_{19}$ fatty acid methyl esters (FAME) in the Fe-rich NFIF bands and in bulk MFIF, while the Si-rich NFIF bands contain mainly $\text{C}_{12}\text{-C}_{21}$ FAMEs, suggesting either selective preservation (lipid recovery was lower in the Fe-rich MFIF bands) or shifts to different potential biological populations during the deposition of the different layers. Preserved lipids discriminate against typical microbial lipid biomarkers like hopanoids, while C_3 plant FAME are detected in all studied materials (Fig. 15). However, the anaerobic bacteria indicator, $10\text{MeC}_{16:0}$ FAME, was identified in a few bands.

539

540 **4 Discussion**

541 **4.1 Sedimentological processes**

542 The three sub-basin division of the CVSB is consistent with previous proposals
543 suggesting that sedimentation within the CVSB was characterized by active
544 synvolcanic rifting which must have been important in shaping basin topography and
545 the creation of sub-basin architecture (Papanikolaou et al., 1990; Stewart and McPhie,
546 2006; Liakopoulos et al., 2001; Papavassiliou et al., 2017). Moreover, this tectonic
547 regime would suggest that the location(s) of volcanism were continually changing
548 relative to the two stratigraphic sections, which themselves were also being affected,
549 i.e. changes in depositional water depth and sedimentation style or and/or that local
550 submarine or subaerial topographic highs impeded the lateral continuity of
551 sedimentary units (Stewart and McPhie, 2006). Chi Fru et al. (2015) have suggested
552 there is an upward deepening of the overall depositional setting recorded in the “Little
553 Vani” section, consistent with rifting during CVSB infilling time.

554 The CVSB floored by dacitic/andesitic lava domes and overlain by
555 volcanoclastic infill, dates back to Upper Pliocene-Lower Pleistocene. A complex
556 mosaic of lithologically diverse sedimentary units (blocks), confined by neotectonic
557 marginal faults, characterizes the CVSB (Fig. 2). The most pronounced of these faults
558 being the NW-trending Vromolimni-Kondaros fault (Papanikolaou et al., 1990) that
559 has been proposed as the trigger of the hydrothermal activity that deposited Mn ore in
560 the CVSB (Papanikolaou et al., 1990; Liakopoulos et al., 2001; Alfieris et al., 2013;
561 Papavassiliou et al., 2017). The stratigraphically tight coupling between Mn and Fe
562 deposition, linked by Fe oxide minerals in feeder-veins, and positive Eu anomalies
563 (Fig. 14) indicating vent-sourced Fe (Maynard, 2010), associate Fe mineralization to

564 fault-triggered hydrothermalism in the CVSB. This is consistent with models of
565 geothermal fluid circulation along fault lines as conduits for the Mn-rich fluids that
566 formed the Milos Mn ore deposit (Hein et al., 2000; Liakopoulos et al., 2001; Glasby
567 et al., 2005; Kiliyas, 2011; Papavassiliou et al., 2017). More importantly, the overall
568 complex neotectonic structure of the CVSB (Papanikolaou et al., 1990) would explain
569 the creation of restricted basins, with sedimentological, lithological and geothermal
570 conditions that enabled the development of unique biogeochemical circumstances in
571 which the NFIF and MFIF formed.

572 The presence of the three depositional basins is supported by the fact that the
573 sequence lithologies in each fault-bound unit are characterized exclusively by
574 occurrences of specific and variably thick stratigraphic packages that tend to be
575 absent in others. For example, the MFIF occurs restricted to basin 1 and the NFIF to
576 Basin 3. Basin 2 is further distinguished by 35-50 m thick interbedded ore-grade Mn-
577 mineralized and glauconitic sandstones/sandy tuffs, much less developed in Basins 1
578 and 3 (Fig. 2). The presence or absence of a stratigraphic sequence, together with its
579 thickness variation, are interpreted as a result of local syntectonic sediment formation
580 conditions in each basin as a result of block tectonic movements along fault lines
581 (Papanikolaou et al., 1990). It may also be attributed to unique basin scale water
582 column redox conditions (e.g. Bekker et al., 2010, and references therein), post-
583 depositional erosion and changing sea level stand (Cattaneo & Steel, 2000).

584 The lack of hydrothermal feeder veins or seafloor exhalative structures (i.e.,
585 chimneys) in the MFIF and NFIF lithologies, suggests that hydrothermal Fe(II) was
586 delivered by diffuse flow and that the Milos-IF formed on the seafloor.
587 Further, mineralisation of the MFIF is suggested to have occurred during two major
588 hydrothermal venting stages. The first produced the MFIF and the second

contaminated it with cryptomelane. Cryptomelane in the MFIF is therefore not a replacement product of primary Mn oxides formed during the deposition of the MFIF, because the anoxia prevailing in Basin 1 at the time (Figs 2 & 13C) would have precluded the precipitation of Mn oxide minerals, hinting that a second phase hydrothermal fluid emission rich in dissolved Mn, directly precipitated cryptomelane from solution as a secondary mineral relative to the primary Fe(III)(oxyhydr)oxides in the MFIF. This occurred during an episode when the MFIF deposit must have been exposed to oxygenated fluids, most likely through mixing with seawater at depth, indicated by the abundance of cryptomelane at the base of the MFIF. Our model for cryptomelane precipitation in the MFIF is therefore different from the one suggesting diagenetic transformation of primary Mn ores at Milos (Hein et al., 2001; Liakopoulous et al., 2001; Papavassiliou et al. 2017).

Geomorphological/chemical reconfiguration orchestrated the deposition of the NFIF in a deeper, small-restricted basin (Fig. 2). The deepening of Basin 3 is reflected in the underlying graded conglomerate bed that exhibits an upward fining trend, followed by transition into the fine-grain NFIF. The conglomerate bed may represent rapid deposition during a high-energy event, i.e. storm or mass flow, whereas the upward fining in the bed is better explained by the depositional mechanism losing energy through time. These high-energy conditions apparently must have ceased during the deposition of the overlying NFIF, where we interpret that increased abundance of finely laminated IF and decreased evidence of storm and/or mass flow reworking reflects deepening conditions. The hypothesized deepening of Basin 3 is consistent with the interpretation that active rifting was an important mechanism in the formation of the CVSB (Papanikolaou et al., 1990).

4.2 Formation Mechanism of The Milos BIFs

4.2.1 Paragenetic sequence

It is stressed that the previously generalized model proposed for biological deposition of the Milos IF, refers exclusively to parts of what is now designated as MFIF (Chi Fru et al., 2013). The NFIF is strongly banded, but does not display the typical microfossils seen in the MFIF, where diffused microbanding apparently relates to the distribution of microbial mats in thin sections (Chi Fru et al., 2013, 2015). The distinction of microcrystalline quartz and amorphous silica phases in the MFIF and NFIF, respectively, together with nano-crystalline hematite particles, suggests a primary amorphous silica origin in both deposits, diagenetically transformed to quartz in the MFIF. The difference in silica crystallinity between the IFs is concurrent with the older age predicted for the MFIF relative to the NFIF, from reconstructed sequence stratigraphy (Fig. 2). Hematite in BIFs is generally interpreted, based on thermodynamic stability, to be a transformation of various primary Fe(III) minerals, with ferrihydrite often proposed as the principal precipitate from the water column (Glasby and Schulz, 1999; Bekker et al., 2010; Johnson et al., 2008; Percoits et al., 2009). It is thought that acidic pH yields mainly goethite while hematite is produced at circumneutral pH (Schwertmann and Murad, 2007). The notable absence of diagenetic magnetite and Fe carbonates (siderite and ankerite), point to negligible coupling of primary Fe(III) oxyhydroxides reduction to organic matter oxidation by the dissimilatory iron-reducing bacteria during burial diagenesis (Johnson et al., 2008). Minor occurrence of iron-silicate phases (Chi Fru et al., 2015) indicates an origin of the hematite precursor in seawater independent of the iron silicate proposed in some cases (Fischer and Knoll, 2009; Rasmussen et al., 2013, 2014). The up to 50 wt% Fe content recorded in the Fe-rich bands, indicate that large amounts of

dissolved Fe(II) was intermittently sourced and deposited as primary Fe(III) minerals, through various oxidative processes in the depositional basin.

Importantly, the CIA analysis does not support mass weathering and mineralization of terrestrial Fe and Si, in agreement with the absence of rivers draining into the CVSB (Chi Fru et al., 2013). The specific identification of plant biolipids would at face value imply post-depositional contamination. However, samples were sawn to remove exposed layers and only the laminated bands for the NFIF were analyzed. Modern sediments from Spathi bay, located Southeast of Milos Island where hydrothermal activity is presently ensuing at 12.5 m below sea level, revealed similar plant lipids as recorded in the Quaternary IF (Fig. 15G). Post-depositional contamination with terrestrial plant lipids is therefore ruled out for the idea that recalcitrant plant biomass probably entered the sediments via seawater entrainment at the time of deposition (see Naden et al., 2005). This finding necessitates the careful interpretation of bulk $\delta^{13}\text{C}_{\text{org}}$ values obtained from both the modern and ancient Milos sediments, involving in situ and ex situ biological contributions to $^{13}\text{C}_{\text{org}}$ fractionation by various known carbon fixation pathways (Preuß et al., 1989; Berg et al., 2010).

4.2.2 Tectono-sedimentary processes and band formation

Fluctuation in hydrothermal activity is proposed to account for the banding in the NFIF (Fig. 16), under redox depositional conditions inferred to be mainly reducing for both investigated IFs, consistent with previous reports (Chi Fru et al., 2013, 2015). Positive Eu anomalies indicate a hydrothermal origin for all but one of the sample suite (Fig. 14A). However, statistically calculated Eu/Eu* anomalies ($Eu_{(SN)}/(0.66Sm_{(SN)} + 0.33Tb_{(SN)})$) to correct for differences in Gd anomalies commonly

encountered in seawater (Planavsky et al., 2010) are in the range of 0.1-0.58, averaging 0.42. The lack of statistically significant true negative Ce anomalies (Fig. 14B) supported by sequential Fe redox reconstruction (Fig. 3C-D; Planavsky et al., 2010; Poulton and Canfield, 2005, 2011; Guilbaud et al., 2015; Sperling et al. 2015), indicate a reducing depositional environment for both The MFIF and the NFIF.

CIA analyses traditionally provide relative information on contributions from chemical weathering to sediment deposition, linked to operative hydrological and climatological patterns on land. This information is often gleaned from ancient and modern soils and from reworked siliclastic deposits in marine basins (Maynard, 1993; Bahlburg & Dobrzinski, 2011). The calculated CIA values, however, are closer to the range obtained for unweathered and or only minimally weathered volcanic rocks (e.g., Nesbitt & Young, 1982; Bahlburg & Dobrzinski, 2011), thus pointing to a predominantly volcanic and/or hydrothermal provenance for the clastic sedimentary materials in the IFs.

It has been suggested that the release of reduced submarine hydrothermal fluids contributed towards maintaining water column anoxia during the deposition of Precambrian BIFs (Bekker et al., 2010). The calculated Eu anomalies (Fig. 14) and petrographic data showing volcanoclastic detritus (i.e., K-feldspar, sanidine, tridymite, cristobalite) as key rock components are in agreement with a submarine hydrothermal source for the investigated IFs. The coarse volcanoclastic detritus embedded in the Fe-rich bands compared to the finer particles in the Si-rich layers, highlights rapid oxidation of Fe(II) that coincided with periodic cycles of hydrothermal/volcanic discharge of new materials into the water column. However, the fine-grained nature of both the MFIF and NFIF deposits suggests that deposition likely occurred away from where such activity was occurring or that volcanic/hydrothermal discharge of Fe

and Si was non-eruptive and disruptive. The Fe-rich bands repetitively revealed hematite grains cementing the denser volcanoclastic fragments that gradually diminish upwards into a zone of fine-grained hematite before transitioning into Si-rich bands consisting mainly of finer volcanoclastic detritus. These observations provide three valuable interpretational considerations for proposing a model for the formation of the alternating Si and Fe-rich bands.

1. The Si and Fe oxides-rich bands are primary precipitates formed in the water column, by a process in which the precipitation of amorphous Si occurred during quiescent non-volcanic intervals, with the oxidation and precipitation of reduced Fe intermittently introduced into the water column by volcanic/hydrothermal activity to form the Fe oxides.
2. The repetitive zonation of distinct particle sizes, suggests density gradient sedimentation that requires a water column-like environment, rather than diagenetic alteration of pre-formed sediments by hydrothermal fluids.
3. The reducing depositional conditions do not support sediment diagenesis as an alternative model for explaining the origin of the Milos IF. This is because the oxidation of ferrous Fe supplied in reduced hydrothermal fluids, must interact with a sizeable pool of oxygen, enabling microaerophilic bacteria oxidation of ferrous iron to Fe(III)(oxyhydr)oxides (Johnson et al., 2008). Otherwise, light-controlled photoferrotrophy, an extremely rare sediment characteristic, precipitates Fe oxides in the absence of oxygen in sunlight environments (Weber et al., 2006).

4.2.3 Biological involvement

Hematite precipitation in the MFIF on microbial filaments (Chi Fru et al., 2013) was previously used to propose a generalized basin-scale mechanism for the deposition of Fe-rich rocks in Cape Vani. However, such filaments are absent in the NFIF, while pure hematite grains are tightly bound to relics of an organic matter signal carrying a maximum $\delta^{13}\text{C}_{\text{org}}$ signature of -25‰ (Table 2). Similar processes are recorded in modern marine sediments where interactions between Fe and free organic matter has been reported to enable the preservation up to 21.5wt% of total organic carbon over geological time scales (Lalonde et al., 2012). Moreover, Fe generally traps and preserves organic matter at redox interfaces (Riedel et al., 2013). The data appear to suggest that the mechanism of Fe(III) (oxyhydr)oxide precipitation and preservation varied between the two IFs. The photoferrotrophic-like filamentous fossils reported in the MFIF (Chi Fru et al., 2013), are absent in the NFIF. This does not, however, rule out the potential role of microbial involvement in Fe(II) oxidation, as diverse microbial taxa carry out this process, several of which are non-filamentous (Chi Fru et al., 2012). However, our data is insufficient to enable clear quantification of the levels of abiotic vs. biotic contribution to Fe(II) oxidation in the NFIF. Nevertheless, the inferred predominantly anoxic depositional conditions as explained above, together with the identification of anaerobic bacteria biomarkers in the laminated bands, intuitively favor significant contribution of anaerobic biological Fe(II) oxidation in the precipitation of primary Fe(III)(oxyhydr)oxides in the NFIF. See Weber et al., 2006, for a review of potential biological pathways to anaerobic Fe(II) oxidation.

Briefly, anaerobic microbial Fe(II) oxidation can proceed via nitrate reduction and by photoferrotrophy to deposit Fe(III)(oxyhydr)oxides. These mechanisms have been linked to microbial contribution to BIF formation (Weber et al., 2006; Kappler et al., 2005) and also for the MFIF (Chi Fru et al., 2013). However, it is also possible

that microaerophilic neutrophilic Fe(II)-oxidizing bacteria likely played an important role, assuming a depositional setting analogous to the Santorini caldera and Kolumbo shallow submarine volcanoes, where such low-O₂-dependent microbial Fe(II) oxidation has been identified to actively precipitate Fe(III) (oxyhydr)oxides (Kiliass et al., 2013b; Camilli et al., 2015). It appears that in the MFIF, precipitating Fe(III)(oxyhydr)oxide minerals were bound and preserved free of organic carbon or that such organic carbon was diagenetically degraded. As was previously shown, Fe(III)(oxyhydr)oxides completely replaced the organic content of the filamentous microfossils in the MFIF (Chi Fru et al., 2013).

The 10MeC_{16:0} FAME identified in the rocks has been reported in anaerobic organisms coupling nitrite reduction to methane oxidation (Kool et al., 2012), in sulfate and iron-reducing bacterial species such as *Desulfobacter*, *Desulfobacula* (Bühning et al., 2005; Dowling et al., 1986; Taylor and Parkes, 1983), *Geobacter*, *Marinobacter* and the marine denitrifier, *Pseudomonas nautical* (Kool et al., 2006; Bühning et al., 2005; Dowling et al., 1986). It had previously been proposed that post-depositional denitrification was a potential pathway for early organic matter removal, justified by the low rock organic carbon and nitrogen content in the Milos BIF-type rocks (Chi Fru et al., 2013, 2015; Table 2). Equally, the detected 10MeC_{16:0} FAME has also been found in anaerobic oxidation of methane (AOM) communities (Alain et al., 2006; Blumenberg et al., 2004), originating from sulfate reducing bacteria. However, bulk sediment $\delta^{13}\text{C}_{\text{org}}$ of -20‰ does not reflect AOM activity that is expected to produce bulk $\delta^{13}\text{C}_{\text{org}}$ values that are $\leq -30\text{‰}$. Low 10MeC_{16:0} FAME concentrations frustrated attempts at acquiring its compound specific isotopic signature to enable further biomolecular level reconstruction of active microbial metabolisms to explain Fe deposition mechanisms.

It is nevertheless puzzling why potential microbial biomarkers typical of marine or hydrothermal vent environments are hardly preserved in the rocks, given that microfossil evidence indicates a vast community of diverse prokaryotic assemblages in the adjacent MFIF (Chi Fru et al., 2013, 2015). Moreover, sediments of the modern Milos hydrothermal system and elsewhere on the HVA, are ubiquitously colonized by microbial life, characterized by the marked large-scale absence or low abundance of higher life forms, including plants (Kiliass et al., 2013b; Camilli et al., 2015; Oulas et al., 2015). One possibility could be the discriminatory preservation of lipids related to their selectivity and reactivity towards Fe(III)(oxyhydr)oxides and clays or different pathways to diagenetic degradation (e.g., Canuel & Martens, 1996; Lü et al., 2010; Riedel et al., 2013). As noted, the carbonaceous materials in the BIF-type NFIF rocks occur in tight association with hematite.

Importantly, prokaryotic biomarkers are suggested to poorly preserve in these young BIF analogues. This raises the possibility that this may provide an important explanation for why lipid biomarkers are yet to be extracted from Precambrian BIFs. Moreover, the data are compatible with the low C_{org} recorded in BIFs of all ages, suggesting that the low C_{org} abundance may not be due to metamorphism as often proposed (Bekker et al., 2010) or to C_{org} oxidation by dissimilatory iron reducing bacteria to form ^{13}C -depleted siderite and ankerite during diagenesis (Johnson et al., 2008; Bekker et al., 2010). The Milos BIF-type rocks are unmetamorphosed and lack iron carbonate, yet have vanishingly low C_{org} levels similar to the ancient metamorphosed BIFs. However, an alternative possibility is that the iron oxides may have been reduced through biological oxidation of organic carbon, but carbonate saturation was not reached (Smith et al., 2013).

788

789 **4.2.4 Mn layers and the deposition of the Si-Fe-rich facies**

790 Cryptomelane $[K(Mn^{4+}, Mn^{2+})_8O_{16}]$, which commonly occurs in oxidized Mn
791 deposits resulting from mineral replacement and as open space fillings (Papavassiliou
792 et al., 2016), is also common in the MFIF. This supports the idea of post-depositional
793 impregnation of the base of the MFIF by Mn-rich fluids. Microscopic analysis
794 supports the epigenetic origin of the Mn in the MFIF by revealing Mn oxides growing
795 along fractures, impregnating and replacing Fe minerals (Fig. 4B-F). The
796 macroscopically evident thinning out to disappearance of such Mn-rich horizons up
797 the MFIF, coupled by their development along microfractures emphasizes this
798 epigenetic origin. Mn is not a common feature of the NFIF, even though it sits on top
799 of a thin sandstone layer that is highly mineralized with Mn, locally forming the cap
800 of the main Mn ore at Cape Vani. The generally accepted view is that Mn-rich
801 hydrothermal fluids rose and mineralized the Cape Vani sandstones (Hein et al., 2000;
802 Liakopoulos et al., 2001; Glasby et al., 2005). Based on the stratigraphic location of
803 the MFIF, which pre-dates the Mn-rich sandstones, it is proposed that impregnation of
804 the MFIF by Mn was coeval with large-scale Mn ore mineralization of the Cape Vani
805 sandstones, implying the entire basin was likely oxygenated at the time. The lack of
806 Ce anomalies, confirmed by the sequential Fe extraction proxy data, suggests that
807 both the MFIF and the NFIF formed in anoxic settings. Similar data for the Mn oxides
808 have suggested formation in oxic settings (Glasby et al., 2005; Chi Fru et al., 2015).
809 This implies that Mn epigenetically replaced the MFIF, either because the basin was
810 tectonically uplifted into a high-energy oxygenated shallow water setting or that sea
811 level dropped, leading to partial metasomatism of the base of MFIF, when oxygenated
812 seawater mixed with reduced hydrothermal fluids and precipitated Mn. The lack of

significant Ce anomalies in the dataset, combined with the inferred deepening of basin 3 and the anoxic depositional conditions suggested by the sequential iron redox proxy, further indicate that for the final deposition of the NFIF, an eventual deepening event must have been triggered, resulting in deoxygenation of parts of the CVSB.

All of this is feasible with the three-basin-fault-bounded hypothesis as a requirement for movement along fault lines in response to temporal tectonic activation. The upward sequence transition from the Mn-rich sandstone facies, through the pebbly conglomerate and the final termination in the overlying mud-grained NFIF (Fig. 8B), reflect sedimentary features formed during multiple changes in seawater levels (Cattaneo & Steel, 2000)..

Uplifting is suggested by potential weathering of the NFIF to form the ferruginous duricrust cap. Comparable ferruginous layers on Precambrian BIFs are linked to pervasive subaerial chemical weathering, via the dissolution of the silica-rich layers and precipitation of relatively stable Fe oxides in the spaces between more resistant hematite crystals (e.g., Dorr, 1964; Shuster et al., 2012; Levett et al., 2016). This collective evidence supports the existence of a geodynamic tectonic system capable of producing shallow oxic to deeper anoxic basin conditions at different times that would explain the existence of Mn and Fe oxide layers within the same sedimentary sequence. For example, it is common knowledge that both Fe and Mn oxides will precipitate in the presence of oxygen (Roy, 1997, 2006), with kinetic rates usually being faster for the oxidation of reduced Fe than reduced Mn. In the Fe(II)-rich conditions that prevail in anoxic settings, abiotic reactions between Fe(II) and Mn oxides, produce Fe(III) leading to the dissolution of the Mn oxides to form reduced Mn, implying Mn oxides should not accumulate (Dieke, 1985). Moreover, under these conditions, biological precipitation of Fe(III) can occur rapidly, leaving dissolved Mn

in solution to be deposited when oxygen becomes available. Given that the hydrothermal fluids of the Hellenic Volcanic Arc are commonly enriched in both reduced Fe and Mn, the deposition of the MFIF and NFIF therefore implies there was an existing mechanism that enabled the kinetic discrimination and deposition of the oxides of Fe and Mn into separate settings, most likely dependent on prevailing redox conditions. The accumulation of the ferruginous duricrust layer, overprinted by redox sensitive Mn-nodules, above the NFIF indicates a new shallowing event might have terminated the formation of the NFIF.

4.2.5 Modern analogues on the HVA

Mechanistic explanation for the development of potential stratified waters and reducing conditions during the deposition of the Milos BIF is problematic. However, evidence is available from present shallow submarine hydrothermal analogues in the central part of the HVA, to which the CVSB belongs. These include:

(1) The crater floor of the Kolumbo shallow-submarine volcano (~600×1200 m), which rises from 504 to 18 m below sea level near Santorini, (Sigurdsson et al., 2006; Kiliass et al., 2013b).

(2) The N part of Santorini's submerged caldera walls, which rises from 390 m below sea level to over 300 m above sea level (Druitt et al., 1999; Friedrich et al., 2006; Nomikou et al., 2013; Camilli et al., 2015).

(3) The coastal embayments at the Kameni emergent volcanic islands in the centre of the Santorini caldera (Hanert, 2002; Nomikou et al., 2014; Robbins et al., 2016).

The benthic waters within Kolumbo's crater potentially sustain O₂ depleted conditions via stable CO₂-induced water column densification, and accumulation of

acidic water (pH~5), extending ~10 m above the CO₂ venting crater floor (Kiliyas et al., 2013b). This phenomenon is believed to lead not only to obstruction of vertical mixing of bottom acidic water, but also to O₂ deprivation by precluding efficient transfer of oxygenated surface seawater into the deeper crater layer. In addition, diffuse CO₂ degassing is believed to be linked to the formation of Fe microbial mats and amorphous Fe(III) oxyhydroxides on the entire Kolumbo crater floor (Kiliyas et al., 2013b). Prerequisites for the O₂-depleted conditions to happen are the closed geometry of the Kolumbo crater and the virtually pure CO₂ composition of the released hydrothermal vent fluids that produce O₂ stratification along a stable CO₂-pH gradient.

A similar scenario is reported for the Santorini caldera, where large (~5 m diameter) CO₂-rich, acidic (pH, ~5.93) hydrothermal seafloor pools and flow channels, develop within m-thick microbial Fe-mats on the seafloor slope at 250-230 m below sea level. Persistent hypoxia exists in these pools, representing concentrated seafloor CO₂ accumulation centers generated by hydrothermal venting (Camilli et al., 2015). Here, the dissolved O₂ content (~80 μM or less) in the pools is ~40 % depleted relative to the surrounding ambient seawater (Camilli et al., 2015). These hypoxic conditions are comparable to or even lower than those measured in the CO₂-rich oxygen minimum zones of coastal oceans, relative to seawater existing in equilibrium with atmospheric pO₂ and pCO₂ pressures (Paulmier et al., 2008, 2011; Franco et al., 2014). These conditions enable strong redox stratification of the pool waters, in which unique Si- and Fe-rich microbial mats are associated with amorphous opal and Fe(III)(oxyhydro)xides (Camilli et al., 2015). Importantly, the Fe microbial mats in these CO₂-rich hypoxic pools are affiliated with specific microaerophilic Fe(II)-oxidizing bacteria that accumulate Fe(III) oxyhydroxides (Camilli et al., 2015; Oulas

et al., 2015). These Fe bacteria are implicated in the deposition of the Precambrian BIFs (Konhasuer et al., 2002; Planavsky et al., 2009; Bekker et al., 2010).

Hypoxia is also associated with the water column of the Fe(III)-rich coastal embayments and their hydrothermal vents (≤ 1.0 m water depth), Kameni islands (Hanert, 2002; Robbins et al., 2016 and references therein). Venting fluids are warm (20-40 °C), acidic to circumneutral (pH 5.5-6.9), enriched in CO₂, Fe and Si (Georgalas & Liatsikas, 1936, Boström et al., 1990; Handley et al., 2010; Robbins et al., 2016). Water column stratification is expressed as decreasing O₂ with depth that is positively related to Fe(III)(oxyhydr)oxide density and microaerophilic Fe(II)-oxidizing bacterial prevalence (Hanert, 2002). Robbins et al. (2016) found that Fe(III)-rich suspended particulate material in these “Fe bays” may be associated with anoxia, extending up to the air-seawater interface, near the hydrothermal vents (Hanert, 2002). They consist of ferrihydrite, goethite and microaerophilic Fe(II) oxidizers.

However, the biogeochemical occurrence of these phenomena within the localized confines of the Santorini caldera and Kolumbo crater, may however be difficult to achieve in ordinary shallow submarine hydrothermal settings, such as those occurring on the coast of present day Milos. The same may be true for Tatum Bay, where non-volcanic and unconfined diffuse hydrothermalism is widespread (Dando et al., 1996; Pichler & Dix, 1996; Pichler & Veizer, 1999; Stüben et al., 1999; Rancourt et al., 2001; Varnavas et al., 2005).

In the Kolumbo and Santorini hydrothermal fields, benthic pH averages 5.5 and the deposition of carbonates is markedly absent (Kiliass et al., 2013b, Camilli et al., 2015; Robbins et al., 2016). This conforms to observations in the MFIF and NFIF units where carbonate mineralization is not detected, thereby suggesting a similar low pH

depositional environment for both the MFIF and NFIF. Ubiquitous Fe(III)(oxyhydr)oxide precipitation and enriched Si content are prevalent in the CO₂-rich-hypoxic shallow submarine Santorini caldera slope pools and the Kameni Fe-embayments where sulfide precipitation is inhibited (Camilli et al., 2015), or extremely rare (Robbins et al., 2016). Such sulfide-poor conditions are critical for the formation of BIFs (Bekker et al., 2010).

A high Si-Fe(III)(oxyhydr)oxide content, absence of carbonate and sulfide mineralization, coupled to a generally low S content have also been demonstrated for the CVSB Fe formations (Chi Fru et al., 2013, 2015). This depositional situation is different, for example, from the unconfined shallow submarine hydrothermal systems in Tatum Bay and Bahia Concepcion Bahia California Sur, Mexico, where authigenic carbonate deposition is widespread (Canet et al., 2005; Pichler & Veizer, 1996, 2005). Moreover, there is strong geological evidence that within volcanic crater environments associated with high CO₂ emission, long-term water column redox stratification is possible under these special conditions. Further evidence is found in volcanic crater lakes (for example the shallow 205 m deep lake Nyos in Cameroon—renowned as one of Earth’s three CO₂ saturated volcanic lakes (Ozawa et al., 2016; Kling et al., 2005). Here CO₂-induced water column stratification is associated with bottom reducing conditions characterized by a low sulfate and high Fe bottom water content relative to surface concentrations (Tiodjio et al., 2014).

5 Concluding remarks

This study shows the following new insights in light of what was previously known:

1. At least two distinct IFs (MFIF and NFIF) formed from hydrothermal mud, within two localized sub-basins in the ~1 km-long CVSB, ~2.66-1.0 Myr ago, controlled by local tectonism.
2. Local conditions of elevated and cyclic supply of ferrous Fe and dissolved Si, accompanied by strict bottom water anoxic conditions in a localized reservoir cut off from the open ocean, can in principle allow the deposition of BIF-type rocks in a modern marine setting. The rarity of these types of deposits however suggests that such conditions are extremely difficult to attain under the modern oxygen-rich atmosphere.
3. A working model that band formation may involve potential Fe(III)(oxyhydr)oxide filling of sediment pores and fractures during diagenesis, is not supported by the data. In addition to the lack of observation of such phenomena, as demonstrated for replacive Mn mineralization, calculated Ce and Eu anomalies, together with preliminary sequential iron extraction analysis (Poulton and Canfield, 2011; data not shown), are suggestive of anoxic depositional conditions likely induced by the release of reduced hydrothermal/volcanic fluids into a cutoff sedimentary basin.
4. The precipitation of Fe(III) and Mn oxides require oxygen. In the absence of oxygen, Mn is not oxidized, while light and photoferrotrophy will oxidize reduced Fe to Fe(III)(oxyhydr)oxides. Both light and photoferrotrophy are however extremely rare characteristics of anoxic sediments, but a common feature of anoxic Fe²⁺-rich waters, where photoferrotrophy is widespread (Weber et al., 2006). Collectively, these observations provide an important feasible mechanism for the knife sharp separation of the Mn oxide-rich ores in the CVSB that are also Fe(III)(oxyhydr)oxide-rich, from the highly

961 localized MFIF and NFIF deposits that are Fe(III)(oxyhydr)oxide-rich but Mn
 962 oxide-poor.

963 5. The mechanism of formation of the MFIF and NFIF therefore most likely
 964 involved exhalative release of reduced hydrothermal/volcanic fluids into a
 965 restricted and deoxygenated seafloor water column where the oxidation of
 966 reduced Fe to Fe(III)(oxyhydr)oxides occurred, most likely by the activity of
 967 photoferrotrophs (Chi Fru et al., 2013). Microaerophilic oxidation of Fe(II)
 968 was likely critical, but that remains to be shown.

969 6. Episodic intensification of hydrothermal activity is identified as a main
 970 mechanism for the formation of the millimetric BIF bands, adding to the
 971 biological mechanism that was inferred from fossil records in the MFIF (Chi
 972 Fru et al., 2013, 2015).

973 7. Abiotic Si precipitation was apparently much slower relative to Fe(III)
 974 precipitation, resulting in Fe-rich bands in the NFIF forming in association
 975 with large fragments of volcanoclast and the Si-rich bands with finer Si grains.

976 8. A combination of the above processes produced pulses of Si and Fe in the
 977 millimetric Si and Fe-rich bands in the NFIF.

978 9. The Milos rocks fulfill sedimentological, chemical and mineralogical
 979 characteristics that established them as potentially the youngest known BIFs;
 980 following the simplistic definition that BIFs are sedimentary rocks composed
 981 of alternating layers of Fe and Si containing at least 15% Fe.

982 10. Whether the rocks described here are analogues of Precambrian BIFs or not,
 983 and whether the proposed formation mechanisms match those that formed the
 984 ancient rocks, is opened to debate. However, there are many similarities to
 985 proposed Precambrian BIF depositional models (e.g. Klien, 2005; Beukes and

Gutzmer, 2008; Smith et al., 2013; Bekker et al., 2010; Klein and Beukes, 1992). Importantly, the present study provides mechanisms by which rocks with alternating Fe and Si-rich bands can be formed in the modern ocean.

Data availability. Data can be accessed by request from any of the authors

Author contributions. ECF, SK and MI designed the study. ECF, SK, KG and MI performed fieldwork. ECF, JER, KG, IM and QH performed research. ECF, SK, KG, MI, QH and JER interpreted data. ECF and SK wrote paper.

Competing interests. The authors declare that they have no conflict of interest.

Acknowledgments. Ariadne Argyraki, Nicole Posth, Nolwenn Callac and Eva Zygouri are acknowledged field assistance during sampling and for stimulating intellectual discussions. Special thanks to Christoffer Hemmingsson for contributing to the SEM and XRD analyses. This work is funded by the European Research Council grant No. 336092 to ECF and the Swedish Research Council grant No. 2012-4364 to MI.

References

Alain, K., Holler, T., Musat, F., Elvert, M., Treude, T., and Kruger M.; Microbiological investigation of methane- and hydrocarbon-discharging mud volcanoes in the Carpathian Mountains, Romania. *Environ. Microbiol.*, 8, 574–590, 2006.

1010 Alfieris, D. and Voudouris, P.: Ore mineralogy of transitional submarine magnatic-
1011 hydrothermal deposits in W. Milos Island, Greece. *Bul. Acad. Sci.*, 43, 1–6, 2005.

1012 Alfieris, D.: Geological, geochemical and mineralogical studies of shallow submarine
1013 epithermal mineralization in an emergent volcanic edifice, at Milos Island (western
1014 side), Greece. PhD thesis, Department Geowissenschaften der Universität
1015 Hamburg, 2006.

1016 Alfieris, D., Voudouris, P., and Spry, P.: Shallow submarine epithermal Pb–Zn–Cu–
1017 Au–Ag–Te mineralization on western Milos Island, Aegean Volcanic Arc, Greece:
1018 Mineralogical, geological and geochemical constraints. *Ore Geol. Rev.*, 53, 159–
1019 180, 2013.

1020 Anand, R. R., Paine, M., and Smith, R.E.: Genesis, Classification and Atlas of
1021 Ferruginous Materials, Yilgarn Craton. CRC LEME Open File Report vol. 13,
1022 CSIRO Exploration and Mining, Perth, 2002.

1023 Bahlburg, H. and Dobrzinski, N.: A review of the Chemical Index of Alteration (CIA)
1024 and its application to the study of Neoproterozoic glacial deposits and climate
1025 transition. *Geol. Soc. London Mem.*, 36, 81–92, 2011.

1026 Bau, M. and Dulski, P.: Distribution of yttrium and rare- earth elements in the Penge
1027 and Kuruman Iron-Formations, oxidative scavenging of cerium on hydrous Fe
1028 oxide, Transvaal Supergroup, South Africa. *Precambrian Res.*, 79, 37–55, 1996.

1029 Berg, I.A., Kockelkorn, D., Ramos-Vera, W.H., Say, R.F., Zarzycki, J., Hügler, M.,
1030 Alber, B.E., and Fuchs, G.: Autotrophic carbon fixation in archaea. *Nat. Rev.*
1031 *Microbiol.*, 8, 447–460, 2010.

1032 Bekker, A., Slack J.F., Planavsky, N., Krapež B., Hofmann, A., Konhauser, K.O., and
1033 Rouxel, O.J.: Iron formation: The sedimentary product of a complex interplay

1034 among mantle, tectonic, oceanic, and biospheric processes. *Econ. Geol.*, 105, 467–
 1035 508, 2010.

1036 Beukes, N.J., and Gutzmer, J.: Origin and Paleoenvironmental significance of major
 1037 Iron Formations at the Archean-Paleoproterozoic boundary. *Econ. Geol.* 15, 5–47,
 1038 2008.

1039 Beukes, N.J., Swindell, E.P.W., Wabo, H.: Manganese deposits of Africa, *Episodes* v.
 1040 39, 285–317, 2016.

1041 Blumenberg, M., Seifert, R., Reitner, J., Pape, T., and Michaelis, W.: Membrane lipid
 1042 patterns typify distinct anaerobic methanotrophic consortia. *Proc. Natl. Acad. Sci.*
 1043 U.S.A., 101, 11111–11116, 2004.

1044 Boström, K., Honnorez, J., Joensuu, O., and Rydell, H.: Chemistry of hydrothermal
 1045 solutions in drill hole GPK-1, Palaea Kameni, Santorini, Greece. *Proceedings of*
 1046 *the third international congress, Santorini, Greece.* 3, 257–260, 1990.

1047 Bronn, H.G.: *Übersicht der Fossilen Überreste in den tertiären subappeninischen*
 1048 *Gebirgen. Italiens Tertiär-Gebilde und deren organische Einschlüsse.* Heidelberg
 1049 pp. XII + 176 + 1 pl, 1831.

1050 Bouma, A.H.: *Sedimentology of Some Flysch Deposits.* Amsterdam, Elsevier, pp.
 1051 168, 1962.

1052 Breitzkreuz, C.: Spherulites and lithophysae—200 years of investigation on
 1053 hightemperature crystallization domains in silica-rich volcanic rocks. *Bull.*
 1054 *Volcanol.*, 75, 1–16, 2013.

1055 Bühring, S.I., Elvert, M., and Witte, U.: The microbial community structure of
 1056 different permeable sandy sediments characterized by the investigation of bacterial
 1057 fatty acids and fluorescence in situ hybridization. *Environ. Microbiol.*, 7, 281–293,
 1058 2005.

1059 Camilli, R., Noumikou P., Escartin, J., Ridao, P., Mallios, A., Kiliyas, S.P., Argyraki,
 1060 A., and the Caldera Science Team: The Kallisti Limnes, carbon dioxide
 1061 accumulating subsea pools. *Sci. Rep.*, 5, 12152, doi:10.1038/srep12152.
 1062 Canuel, E.A. and Marten, C.S.: Reactivity of recently deposited organic matter:
 1063 Degradation of lipid compounds near the sediment-water interface. *Geochim.*
 1064 *Cosmo. Acta*, 60, 1793–1806, 1996.
 1065 Canet, C., Prol-Ledesma, R.M., Torres-Alvarado, I., Gilg, H.A., Villanueva, R.E., and
 1066 Cruz, R.L.S.: Silica-carbonate stromatolites related to coastal hydrothermal venting
 1067 in Bahia Concepcion, Baja California Sur, Mexico. *Sed. Geol.*, 174, 97–113, 2005.
 1068 Cattaneo, A. and Steel, R.J.: Transgressive deposits: a review of their variability.
 1069 *Earth Sci. Rev.*, 62, 187–228, 2003.
 1070 Chi Fru, E., Ivarsson, M., Kiliyas, S.P., Bengtson, S., Belivanova, V., Marone, F.,
 1071 Fortin, D., Broman, C., and Stampanoni, M.: Fossilized iron bacteria reveal a
 1072 pathway to the origin banded iron formations. *Nat. Comm.*, 4, 2050 DOI:
 1073 10.1038/ncomms3050, 2013.
 1074 Chi Fru, E., Ivarsson, M., Kiliyas, S.P., Frings, P.J., Hemmingsson, C., Broman, C.,
 1075 Bengtson, S. and Chatzitheodoridis, E.: Biogenicity of an Early Quaternary iron
 1076 formation, Milos Island, Greece. *Geobiology*, 13, 225–44, 2015.
 1077 Dando, P.R., Hughes, J.A., Leahy, Y., Niven, S.J., Taylor, L.J. and Smith, C.: Gas
 1078 venting rates from submarine hydrothermal areas around the island of Milos,
 1079 Hellenic Volcanic Arc. *Cont. Shelf Res.*, 15, 913–925, 1995.
 1080 Dieke, P. Concentration of Mn and separation from Fe in sediments—I.
 1081 Kinetics and stoichiometry of the reaction between birnessite and
 1082 dissolved Fe(II) at 10°C. *Geochim. Cosmo. Acta*, 49, 1023–1033, 1985.

1083 Dorr, J.V.N.: Supergene iron ores of Minas Gerais, Brazil. *Econ. Geol.*, 59, 1203,
1084 1964.

1085 Dowling, N.J. E., Widdel, F., and White, D.C.: Phospholipid ester-linked fatty-acid
1086 biomarkers of acetate-oxidizing sulfate-reducers and other sulfide-forming
1087 bacteria. *J. Gen. Microbiol.*, 132, 1815–1825, 1986.

1088 Druitt, T. H. L., Edwards, R. M., Mellors, D. M., Pyle, R. S. J., Sparks, M., Lanphere,
1089 M. D., and Barreirio, B.; Santorini Volcano. *Geol. Soc. Mem. London*, 19, 165,
1090 1999.

1091 Fischer, W.W. and Knoll, A.H.: An iron shuttle for deepwater silica in Late Archean
1092 and early Paleoproterozoic iron formation. *Geol. Soc. Am. Bull.*, 121, 222–235,
1093 2009.

1094 Franco, A.C., Hernández-Ayón, J.M, Beie,r E., Garçon, V., Maske, H., Paulmier, A.,
1095 Färber-Lorda, J., Castro, R., and Sosa-Ávalos, R.: Air-sea CO₂ fluxes above the
1096 stratified oxygen minimum zone in the coastal region off Mexico. *J. Geophy. Res.*,
1097 119, 2923–2937, 2014.

1098 Friedrich, W.L., Kromer, B., Friedrich, M., Heinemeier, J., Pfeiffer, T., and Talamo,
1099 S.: Santorini eruption radiocarbon dated to 1627-1600 BC. *Science*, 312, 548–548,
1100 2006.

1101 Fytikas, M., Innocenti, F., Kolios, N., Manetti, P., Mazzuoli, R., Poli, G., Rita, F., and
1102 Villari, L.: Volcanology and petrology of volcanic products from the island of
1103 Milos and Neighbouring islets. *J. Vol. Geotherm. Res.*, 28, 297–317, 1986.

1104 Galan, L.D.P., Doval, M., La Iglesia, A., Soriano, J., and Chavez, L.: Occurrence of
1105 silica polymorphs nanocrystals in tuffaceous rocks, Province of the Mesa Central,
1106 Mexico, and their formation from subcritical Si-rich fluids. *Am. Mineral.*, 98, 977–
1107 985, 2013.

1108 Georgalas, G., and Liatsikas, N.: Die Historische entwicklung des Dafni-Ausbruches
 1109 1925-1926. In Santorin, Der Werdegang eines Inselvulkans und sein Ausbruch
 1110 1925-1928, V. 2 (ed. Reck, H.). Verlag von Dietrich Reimer, Berlin, 1–96 pp,
 1111 1936.

1112 Glasby, G.P. and Schulz, H.D.: Eh, pH diagrams for Mn, Fe, Co, Ni, Cu and As under
 1113 seawater conditions: application of two new types of the Eh, pH diagrams to the
 1114 study of specific problems in marine geochemistry. *Aquatic Geochem.*, 5, 227–
 1115 248, 1999.

1116 Glasby, G.P., Papavassiliou, C.T., Mitsis, J., and Valsami-Jones, E.: The Vani
 1117 manganese deposit, Milos island, Greece: A fossil stratabound
 1118 Mn–Ba–Pb–Zn–As–Sb–W-rich hydrothermal deposit. *Develop. Volcanol.*, 7,
 1119 255–291, 2005.

1120 Gromet, L.P., Dymek, R.F., Haskin, L.A., and Korotev, R.L.: The North American
 1121 shale composit: Its compilation and major trace element characteristics. *Geochim.*
 1122 *Cosmo. Acta*, 48, 2469–2482, 1984.

1123 Gross, G.A.: A classification of iron-formation based on depositional Environments.
 1124 *Can. Min.*, 18, 215–222, 1980.

1125 Guilbaud, R., Poulton, S.W., Butterfield, N.J., Zhu, M., and Shields-Zou, G.A.: A
 1126 global transition to ferruginous conditions during the early Neoproterozoic. *Nat.*
 1127 *Geosci.* 8:466–470, 2015.

1128 Handley, K. M., Boothman, C., Mills, R. A., Pancost, R. D., and Lloyd, J. R.:
 1129 Functional diversity of bacteria in a ferruginous hydrothermal sediment. *ISME J.*,
 1130 4, 1193-1205, 2010.

1131 Hanert, H. H.: Bacterial and chemical iron oxide deposition in a shallow bay on
 1132 Palaea Kameni, Santorini, Greece: microscopy, electron probe microanalysis, and
 1133 photometry of in situ experiments. *Geomicrobiol. J.*, 19, 317–342, 2002.
 1134 Hein, J. R., Stamatakis, M. G., and Dowling, J. S.: Trace metal-rich Quaternary
 1135 hydrothermal manganese oxide and barite deposit, Milos Island, Greece. *Applied*
 1136 *Earth Science: Trans. Inst. Min. Metal. Section B.*, 109, 67–76, 2000.
 1137 Horwell, C.J., le Blond, S., Michnowicz, S. A. K. and Cressey, G.: Cristobalite in a
 1138 rhyolitic lava dome: evolution of ash hazard. *Bull. Volcanol.* 72, 249–253, 2010.
 1139 Ichihara, K. and Fukubayashi, Y.: Preparation of fatty acid methyl esters for gas-
 1140 liquid chromatography. *J. Lipid Res.*, 51, 635–40, 2010.
 1141 James, H. L.: Sedimentary facies of iron-formation. *Econ. Geol.*, 49, 235–293, 1954.
 1142 Johnson, C. M., Beard, B. L., and Roden, E. E.: The iron isotope fingerprints of redox
 1143 and biogeochemical cycling in modern and ancient Earth. *Ann. Rev. Earth Plan.*
 1144 *Sci.*, 36, 457–493, 2008.
 1145 Kappler, A., Pasquero, C., and Newman, D.K.: Deposition of banded iron formations
 1146 by anoxygenic phototrophic Fe(II)-oxidizing bacteria. *Geology*, 33, 865–868,
 1147 2005.
 1148 Kiliass, S. P., Detsi, K., Godelitsas, A., Typas, M., Naden, J., and Marantos, Y.:
 1149 Evidence of Mn-oxide biomineralization, Vani Mn deposit, Milos, Greece. In:
 1150 Proceedings of the ninth biennial Meeting of the Society for Geology Applied to
 1151 Mineral Deposits, Dublin, Ireland. *Irish Assoc. Econ. Geol.* 1069–1072 pp, 2007.
 1152 Kiliass, S. P.: Microbial mat-related structures in the Quaternary Cape Vani
 1153 manganese-oxide (-barite) deposit, NW Milos island, Greece. *Soc. Sed. Geol. Sp.*
 1154 *Pub.*, 101, 97–110, 2011.

1155 Kiliyas, S. P., Chatzitheodoridis, E., and Lyon, I.: Molecular, chemical and
 1156 morphological evidence for hematite biogenicity at the Quaternary Cape Vani Mn-
 1157 (Ba-Fe) deposit, Milos, Greece. *Bull. Geol. Soc.*, 47, 834-842, 2013a.

1158 Kiliyas, P. S., Nomikou, P., Papanikolaou, D., Polymenakou, P. N., Godelitsas, A.,
 1159 Argyraki, A., Carey, S., Gamaletsos, P., Mertzimekis, T. J., Stathopoulou, E.,
 1160 Goettlicher, J., Steininger, R., Betzelou, K., Livanos, I., Christakis, C., Bell, K. C.:
 1161 and Scoullou, M. New insights into hydrothermal vent processes in the unique
 1162 shallow-submarine arc-volcano, Kolumbo (Santorini), Greece. *Sci. Rep.*, 3,
 1163 doi:10.1038/srep02421, 2013b.

1164 Klein, C.: Some Precambrian banded iron-formations (BIFs) from around the world:
 1165 Their age, geologic setting, mineralogy, metamorphism, geochemistry, and origins.
 1166 *Am. Min.*, 90, 1473–1499, 2005.

1167 Kling, G. W., Evans, W. C., Tanyileke, G., Kusakabe, M., Ohba, T., Yoshida, Y., and
 1168 Hell, J. V.: Degassing Lakes Nyos and Monoun: Defusing certain disaster. *Proc.*
 1169 *Natl. Acad. Sci. U.S.A.*, 102, 14185–14190, 2005.

1170 Klein, C., and Beukes, N.J.: Time distribution, stratigraphy and sedimentologic
 1171 setting, and geochemistry of Precambrian Iron Formation. In Schopf, J. W., and
 1172 Klein, C.: *The Proterozoic Biosphere: A multidisciplinary study*, 139 – 146.
 1173 Cambridge University Press, New York, 1992.

1174 Konhauser, K. O., Planavsky, N. J., Hardisty, D. S., Robbins, L. J., Warchola, T. J.,
 1175 Haugaard, R., Lalonde, S. V., Partin, C. A., Oonk, P. B. H., Tsikos, H., and Lyons,
 1176 T.W.: Iron formations: A global record of Neoarchaeon to Palaeoproterozoic
 1177 environmental history. *Earth Sci. Rev.*, 172, 140-177, 2017.

1178 Krapež, B., Barley, M. E., Pickard, A. L.: Hydrothermal and resedimented origins of
 1179 the precursor sediments to banded iron formations: Sedimentological evidence

1180 from the early Palaeoproterozoic Brockman Supersequence of Western Australia.
 1181 Sedimentology, 50, 979-1011, 2003.

1182 Lalonde, K., Mucci, A., Quellet, A. and G  linas, Y.: Preservation of organic matter in
 1183 sediments promoted by iron. Nature, 483, 198–200, 2012.

1184 Levett, A., Gagen, E., Shuster, J., Rintoul, L., Tobin, M., Vongsvivut, J., Bambery,
 1185 K., Vasconcelos, P., and Southam, G.: Evidence of biogeochemical processes in
 1186 iron duricrust formation. J. South. Am. Earth Sci., 71, 131–142, 2016.

1187 Li, W., Czaja, A. D., Van Kranendonk, M. J., Beard, B. L., Roden, E. E., Johnson, C.
 1188 M.: An anoxic, Fe(II)-rich, U-poor ocean 3.46 billion years ago. Geochim. Cosmo.
 1189 Acta, 120, 65-79, 2013.

1190 Liakopoulos, A., Glasby, G. P., Papavassiliou, C. T. and Boulegue, J.: Nature and
 1191 origin of the Vani manganese deposit, Milos, Greece: an overview. Ore Geol. Rev.,
 1192 18, 181–209, 2001.

1193 L  , D., Song, Q., and Wang, X.: Decomposition of algal lipids in clay-enriched
 1194 marine sediment under oxic and anoxic conditions. Chin. J. Oceanogr. Limnol., 28,
 1195 131–143, 2010.

1196 Marschik, R., Bauer, T., Hensler, A.-S., Skarpelis, N., and H  lzl, S. Isotope
 1197 Geochemistry of the Pb-Zn-Ba(-Ag-Au) Mineralization at Triades-Galana, Milos
 1198 Island, Greece. Res. Geol., 60, 335–347, 2010.

1199 Maynard, J. B.: Chemistry of modern soils as a guide to interpreting Precambrian
 1200 Paleosols. J. Geol., 100, 279–289, 1993.

1201 Maynard, J. B.: The chemistry of manganese ores through time: a signal of increasing
 1202 diversity of earth-surface environments. Econ. Geol., 105, 535–552, 2010.

1203 McLennan, S.B.: Rare earth elements in sedimentary rocks. Influence of provenance
 1204 and sedimentary processes. In: B.R. Lipin and G.A. McKay (Editors),

1205 Geochemistry and Mineralogy of the Rare Earth Elements. Mineralogical Society
 1206 of America, Washington, pp. 169-200, 1989.

1207 Miall, A. D. Lithofacies types and vertical profile models in braided river deposits.
 1208 Can. Soc. Pet. Geol. Mem., 5, 597–604, 1978.

1209 Miall, A. D.: Architectural element analysis: a new method of facies analysis applied
 1210 to fluvial deposits. Earth Sci. Rev., 22, 261–308, 1985.

1211 Morris, R. V., Vaniman, D. T., Blake, D. F., Gellert, R., Chipera, S. J., Rampe, E. B.,
 1212 Ming, D. W., Morrison, S. M., Downs, R. T., Treiman, A. H., Yen, A. S.,
 1213 Grotzinger, J. P., Achilles, C. N., Bristow, T. F., Crisp, J. A., Des Marais, D. J.,
 1214 Farmer, J. D., Fendrich, K. V., Frydenvang, J., Gradd, T. G., Morookian, J.-M.,
 1215 Stolper, E. M. and Schwenzer, S. P.: Silicic volcanism on Mars evidenced by
 1216 tridymite in high-SiO₂ sedimentary rock at Gale crater. Proc. Natl. Acad. Sci.
 1217 U.S.A., 113, 7071–7076, 2016.

1218 Mutti, E.: Turbidite Sandstones. Agip Spe. Pub., 275 pp, 1992.

1219 Nesbitt, H. W. and Young, G. M.: Early Proterozoic climates and plate motions
 1220 inferred from major element chemistry of lutites. Nature, 199, 715–717, 1982.

1221 Nomikou, P., Papanikolaou, D., Alexandri, M., Sakellariou, D., and Rousakis, G.:
 1222 Submarine volcanoes along the Aegean volcanic arc. Tectonophysics, 597–598,
 1223 123–146, 2013.

1224 Nomikou, P., Parks, M. M., Papanikolaou, D., Pyle, D. M., Mather, T. A., Carey, S.,
 1225 Watts, A. B., Paulatto, M., Kalnins, M.L., Livanos, I., and Bejelou, K.: The
 1226 emergence and growth of a submarine volcano: The Kameni islands, Santorini
 1227 (Greece). Geo. Res. J., 1, 8–18, 2014.

1228 Ozawa, A., Ueda, A., Fantong, W. Y., Anazawa, K., Yoshida, Y., Kusakabe, M.,
 1229 Ohba, T., Tanyileke, G., and Hell, J.V. Rate of siderite precipitation in Lake Nyos,
 1230 Cameroon. *Geol. Soc. London Sp. Pub.*, 437, doi.org/10.1144/SP437.13, 2016.
 1231 Papanikolaou, D., Lekkas, E., and Syskakis, D.: Tectonic analysis of the geothermal
 1232 field of Milos Island. *Bull. Geol. Soc. Greece*, 24, 27–46, 1990.
 1233 Papavassiliou, K., Voudouris, P., Kanellopoulos, C., Glasby, G., Alfieris, D., and
 1234 Mitsis, I.: New geochemical and mineralogical constraints on the genesis of the
 1235 Vani hydrothermal manganese deposit at NW Milos island, Greece: Comparison
 1236 with the Aspro Gialoudi deposit and implications for the formation of the Milos
 1237 manganese mineralization. *Ore Geol.*, 80, 594–611, 2017.
 1238 Paulmier, A., Ruíz-Pino, D., and Garçon, V.: The oxygen minimum zone (OMZ) off
 1239 Chile as intense source of CO₂ and N₂O, *Cont. Shelf. Res.*, 28, 2746–2756, 2008.
 1240 Paulmier, A., Ruiz-Pino, D., and Gaçon, V.: CO₂ maximum in the oxygen minimum
 1241 zone (OMZ). *Biogeosciences*, 8, 239–252. doi:10.5194/bg-8-239-2011, 2011.
 1242 Percoits, E., Gingras, M. K., Barley, M. E., Kapper, A., Posth, N. R., and Konhauser,
 1243 K.O.: Petrography and geochemistry of the Dales Gorge banded iron formation:
 1244 Paragenetic sequence, source and implications for palaeo-ocean chemistry. *Pre.*
 1245 *Res.*, 172, 2009.
 1246 Pichler, T. and Dix, G. R. Hydrothermal venting within a coral reef ecosystem,
 1247 Ambitle Island, Papua New Guinea. *Geology*, 50, 435–438, 1996.
 1248 Pichler, T. and Veizer, J.: Precipitation of Fe(III) oxyhydroxide deposits from
 1249 shallow-water hydrothermal fluids in Tutum Bay, Ambitle Island, Papua New
 1250 Guinea. *Chem. Geol.*, 162, 15–31, 1999.

1251 Pichler, T. and Veizer, J. The precipitation of aragonite from shallow-water
 1252 hydrothermal fluids in a coral reef, Tutum Bay, Ambitle Island, Papua New
 1253 Guinea. *Chem. Geol.*, 207, 317–45, 2004.

1254 Planavsky, N., Rouxel, O., Bekker, A., Shapiro, R., Fralick, P., and Knudsen, A.:
 1255 Iron-oxidizing microbial ecosystems thrived in late Paleoproterozoic redox-
 1256 stratified oceans. *Earth Plan. Sci. Letts.*, 286, 2307–242, 2009.

1257 Planavsky, N. J., Bekker, A., Rouxel, O. J., Kamber, B., Hofmann, A., Knudsen, A.
 1258 and Lyons T. W.: Rare earth element and yttrium compositions of Archean and
 1259 Paleoproterozoic Fe formations revisited: New perspectives on the significance
 1260 and mechanisms of deposition. *Geochim. Cosmo. Acta*, 74, 6387–6405, 2010.

1261 Plimer, I. *Milos Geologic History*. Koan Publishing House, Athens, Greece. 261 pp,
 1262 2000.

1263 Poulton, S.W., and Canfield, D.E.: Development of a sequential iron extraction
 1264 procedure for iron: implications for iron partitioning in continentally derived
 1265 particles. *Chem. Geol.* 2014, 209–221, 2005.

1266 Poulton, S.W. and Canfield, D.E.: Ferruginous conditions: A dominant feature of the
 1267 ocean through Earth’s history. *Elements*. 7, 107–112, 2011.

1268 Preuß, A., Schauder, R., Fuchs, G., and Stichler W.: Carbon isotope fractionation by
 1269 autotrophic bacteria with three different CO₂ fixation pathways. *Zeitschrift für*
 1270 *Naturforschung C.*, 44, 397–402, 1989.

1271 Rancourt, D. G., Fortin, D., Pichler, T., and Lamarche, G.: Mineralogical
 1272 characterization of a natural very As-rich hydrous ferric oxide coprecipitate formed
 1273 by mixing of hydrothermal fluid and sea water. *Am. Min.*, 86, 834–851, 2001.

1274 Rasmussen, B., Meier, D. B., Krapež. B., and Muhling, J. R.: Iron silicate
 1275 microgranules as precursor sediments to 2.5-billion-year-old banded iron
 1276 formations. *Geology*, 41, 435–438, 2013.

1277 Rasmussen, B., Krapež, B., and Meier, D. B. Replacement origin for hematite in 2.5
 1278 Ga banded iron formation: Evidence for postdepositional oxidation of iron-bearing
 1279 minerals. *Geol. Soc. Am. Bull.*, 126, 438–446, 2014.

1280 Riedel, T., Zak, D., Biester, H., and Dittmar, T.: Iron traps terrestrially derived
 1281 dissolved organic matter at redox interfaces. *Proc. Nat. Acad. Sci. U.S.A.*, 110,
 1282 10101–10105, 2013.

1283 Robbins, E. I., Kourtidou-Papadeli, C., Iberall, A. S., Nord, Jr, G. L. and Sato, M.:
 1284 From Precambrian Iron-Formation to Terraforming Mars: The JIMES Expedition
 1285 to Santorini. *Geomicrobiol. J.*, 33, 630–645, 2016.

1286 Roy, S.: Manganese Mineralization: Geochemistry and mineralogy of terrestrial and
 1287 marine deposits. *Geol. Soc. Spe. Pub.*, 119, 5–27, 1997.

1288 Roy, S.: Sedimentary manganese metallogenesis in response to the evolution of the
 1289 Earth system. *Earth-Sci. Rev.*, 77, 273–305, 2006.

1290 Rudnick, R. and Gao, S. Composition of the continental crust. In: *Treatise on*
 1291 *Geochemistry*, vol. 3. Elsevier–Pergamon, Oxford, 1–64 pp, 2003.

1292 Shanmugam, G.: Submarine fans: a critical retrospective (1950–2015). *J.*
 1293 *Palaeogeogr.*, 5, 110-184, 2016.

1294 Schwertmann, U. and Murad, E. Effect of pH on the formation of goethite and
 1295 hematite from ferrihydrite. *Clay Clay Min.*, 31, 277–284, 1983.

1296 Shuster, D. L., Farley, K. A., Vasconcelos, P. M., Balco, G., Monteiro, H. S.,
 1297 Waltenberg, K., and Stone, J. O. Cosmogenic ^3He in hematite and goethite from

1298 Brazilian “canga” duricrust demonstrates the extreme stability of these surfaces.
 1299 Earth Plan. Sci. Lett., 329, 41–50, 2012.
 1300 Sigurdsson, H., Carey, S., Alexandri, M., Vougioukalakis, G., Croff, K., Roman, C.,
 1301 Sakellariou, D., Anagnostou, C., Rousakis, G., Loakim, C., Goguo, A., Ballas, D.,
 1302 Misaridis, T., and Nomikou, P. Marine investigations of Greece’s Santorini
 1303 volcanic field. EOS Trans. Am. Geophy. Union, 87, 337–342, 2006.
 1304 Simonson, B. M.: Sedimentological constraints on the origins of Precambrian iron-
 1305 formations. Geol. Soc. Am. Bull., 96, 244–252, 1985.
 1306 Simonson, B. M. and Hassler, S. W.: Was the deposition of large Precambrian iron
 1307 formations linked to major marine transgressions? The J. Geol., 104, 665–676,
 1308 1996.
 1309 Skarpelis, N. and Koutles, T.: Geology of epithermal mineralization of the NW part of
 1310 Milos Island, Greece. In Proceedings of the 5th International Symposium on
 1311 Eastern Mediterranean Geology. (eds. Chatzipetros, A. & Pavlides S). School of
 1312 Geology, Aristotelian University of Thessaloniki, Thessaloniki, Greece. pp. 1449–
 1313 1452, 2004.
 1314 Smith, A.J.B., Beukes, N.J., and Gutzmer, J.: The Composition and depositional environments of
 1315 Mesoarchean Iron Formations of the West Rand Group of the Witwatersrand Supergroup, South
 1316 Africa. Econ. Geol. 108, 111–134, 2013.
 1317 Sperling, E.A., Wolock, C.J., Gill, B.C., Kunzmann, M., Halverson, G.P., Macdonald,
 1318 F.A., Knoll, A.H., and Johnston D.T.: Statistical Analysis of Iron Geochemical
 1319 Data Suggests Limited Late Proterozoic Oxygenation. Nature 523, 451–454, 2015.
 1320 Stewart, A. L. and Mcphie, J.: Facies architecture and Late Pliocene – Pleistocene
 1321 evolution of a felsic volcanic island, Milo, Greece. Bull. Volcanol. 68, 703–726,
 1322 2006.

- 1323 Sun, S., Konhauser, K. O., Kappler, A., and Li, Y.-L.: Primary hematite in
1324 Neoproterozoic to Paleoproterozoic oceans. *GSA Bull.*, 127, 850–861, 2015.
- 1325 Stüben, D. and Glasby, G.P.: Geochemistry of shallow submarine hydrothermal fluids
1326 from Paleohori Bay, Milos, Aegean Sea. *Exp. Min. Geol.*, 8, 273–287, 1999.
- 1327 Swamy, V., Saxena, S. K., Sundman, B., and Zhang, J.: A thermodynamic assessment
1328 of silica phase diagram. *J. Geophys. Res. Solid Earth*, 99, 11787–11794, 1994.
- 1329 Taylor, J., and Parkes, R. J.: The cellular fatty-acids of the sulfate-reducing bacteria,
1330 *Desulfobacter* sp., *Desulfobulbus* sp. and *Desulfovibrio desulfuricans*. *J. Gen.*
1331 *Microbiol.*, 129, 3303–3309, 1983.
- 1332 Tice, M. M. and Lowe, D. R.: The origin of carbonaceous matter in pre-3.0 Ga
1333 greenstone terrains: A review and new evidence from the 3.42 Ga Buck Reef
1334 Chert. *Earth Sci. Rev.*, 76, 259–300, 2006.
- 1335 Tiodjio, R. M., Sakatoku, A., Nakamura, A., Tanaka, A., Fantong, W. Y., Tchakam,
1336 K. B., Tanyileke, G., Ohba, T., Hell, V. J., Kusakabe, M., Nakamura, S., and Ueda,
1337 A.: Bacterial and archaeal communities in Lake Nyos (Cameroon, Central Africa).
1338 *Sci. Rep.*, 4, 6151, DOI: 10.1038/srep06151, 2014.
- 1339 Trendall, A.F.: The significance of iron-formation in the Precambrian stratigraphic
1340 record. *Int. Assoc. Sed. Spe. Pub.*, 33, 33–66, 2002.
- 1341 Tsikos, H., Mathews, A., Erel, Y., and Moore, J.M.: Iron isotopes constrain
1342 biogeochemical redox cycling of iron and manganese in a Palaeoproterozoic
1343 stratified basin. *Earth Planet. Sci. Lett.*, 298, 125–134, 2010.
- 1344 van Hinsbergen, D. J. J., Snel, E., Garstman, S. A., Mărunțeanu, M., Langereis, C. G.,
1345 Wortel, M. J. R., and Meulen Kamp, J. E.: Vertical motions in the Aegean volcanic
1346 arc: evidence for rapid subsidence preceding volcanic activity on Milos and
1347 Aegina. *Mar. Geol.*, 209, 329–345, 2004.

Varnavas, S. P. and Cronan, D. S.: Submarine hydrothermal activity off Santorini and Milos in the Central Hellenic Volcanic Arc: A synthesis. *Chem. Geol.*, 224, 40–54, 2005.

Weber, K. A., Achenbach, L. A., and Coates, J. D.: Microorganisms pumping iron: anaerobic microbial iron oxidation and reduction. *Nat. Rev. Microbiol.*, 4, 752–64, 2006.

Table 1. Results of X-Ray Radiation (XRD) analysis showing major mineralogical compositions. NFIF (non-fossiliferous iron formation) and MFIF (microfossiliferous iron formation), respectively.

Mineral phase	MFIF1	MFIF2	MFIF3	Fe-rich NFIF2A	Si-rich NFIF2B	Fe-rich NFIF2C	Si-rich NFIFD	Fe-rich NFIF2E	Fe-rich NFIF2F
Hematite	+	+	-	+	+	+	+	+	+
Quartz	+	+	+	-	-	-	-	-	-
Sanidine	-	-	-	+	+	+	+	+	+
Tridymite	-	-	-	-	+	+	+	+	+
Cristobalite	-	-	-	+	-	-	-	-	-
Cryptomelane	-	-	+	-	-	-	-	-	-

1372
 1373
 1374
 1375
 1376
 1377
 1378
 1379
 1380
 1381
 1382
 1383
 1384
 1385
 1386
 1387
 1388
 1389
 1390
 1391
 1392
 1393
 1394
 1395
 1396
 1397
 1398
 1399
 1400

1401 Table 2. Stable isotope results. Letters A-F on the NFIF samples represent respective
 1402 bands of the sawn rock in Figure 7E.

Sample	$\delta^{13}\text{C}_{\text{org}}$ vs PDB (‰)	C_{org} (%)	$\delta^{15}\text{N}$ vs air (‰)	N (%)	$\delta^{34}\text{S}$ vs CDT (‰)	S (%)
Fe-rich NFIF2A	-25,63	0,061	nd	0,023	nd	0,01
Si-rich NFIF2B	-25,03	0,109	nd	0,017	nd	0,02
Fe-rich NFIF2C	-24,45	0,068	nd	0,013	nd	0,02
Si-rich NFIF2D	-25,04	0,076	nd	0,015	nd	0,02
Fe-rich NFIF2E	-25,19	0,042	nd	0,009	nd	0,01
Si-rich NFIF2F	-25,49	0,050	nd	0,012	nd	0,03
MFIF1	-25,49	0,087	nd	0,017	nd	0,01
MFIF2	-26,25	0,046	nd	0,005	nd	nd
MFIF3	-25,69	0,041	nd	0,006	nd	nd

ND, Not detected

1403
 1404

1405
 1406
 1407
 1408
 1409
 1410

 1411

 1412

 1413

 1414

 1415

 1416

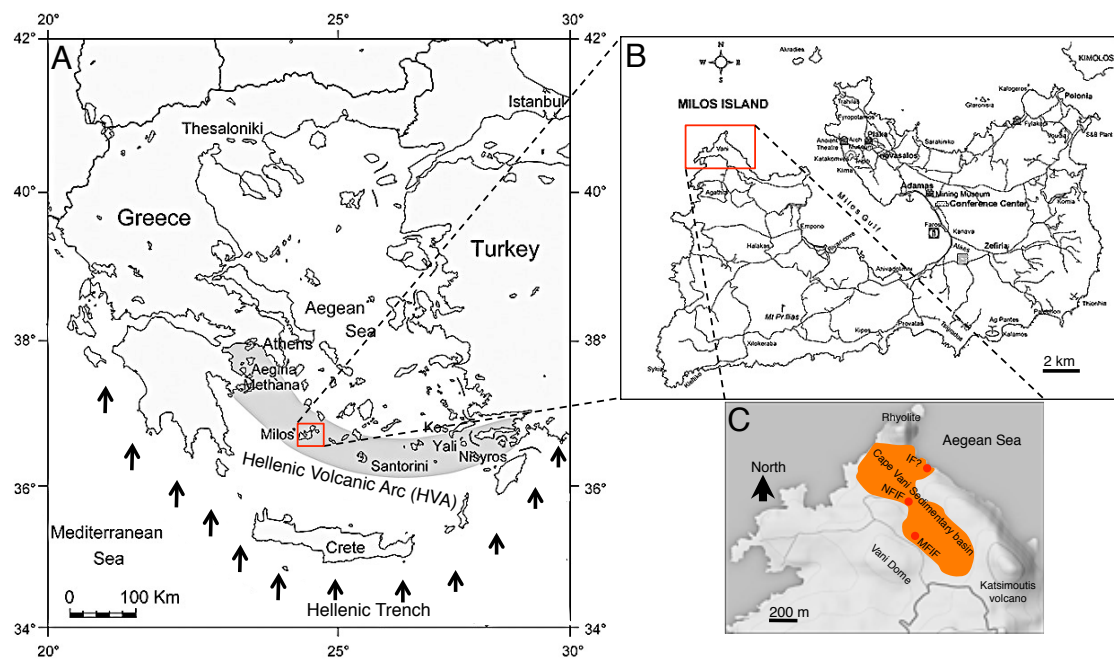
 1417

 1418

 1419

 1420

 1421



1422

1423 Fig. 1. Geological map of Milos (redrawn from Marschik et al., 2010). (A),
 1424 Geotectonic map showing the position of Milos Island, along the Hellenic Volcanic

Arc (HVA). Arrows indicate the direction of subduction of the African plate underneath the Euroasian plate. (B) Milos Island. (C), The Milos iron formation is located in the 8-shaped Cape Vani sedimentary basin (CVSB). At least two IFs are present in the CVSB. These are made up of a non-fossiliferous IF (NFIF) at the juncture between the two large sedimentary basins and a microfossiliferous iron formation (MFIF) located at the SW margin in the second basin. A potential third IF (IF?) is located NE, close to the present day Aegean Sea. It is however not certain if this deposit is part of the NFIF or not, because of the open mining pit separating the two.

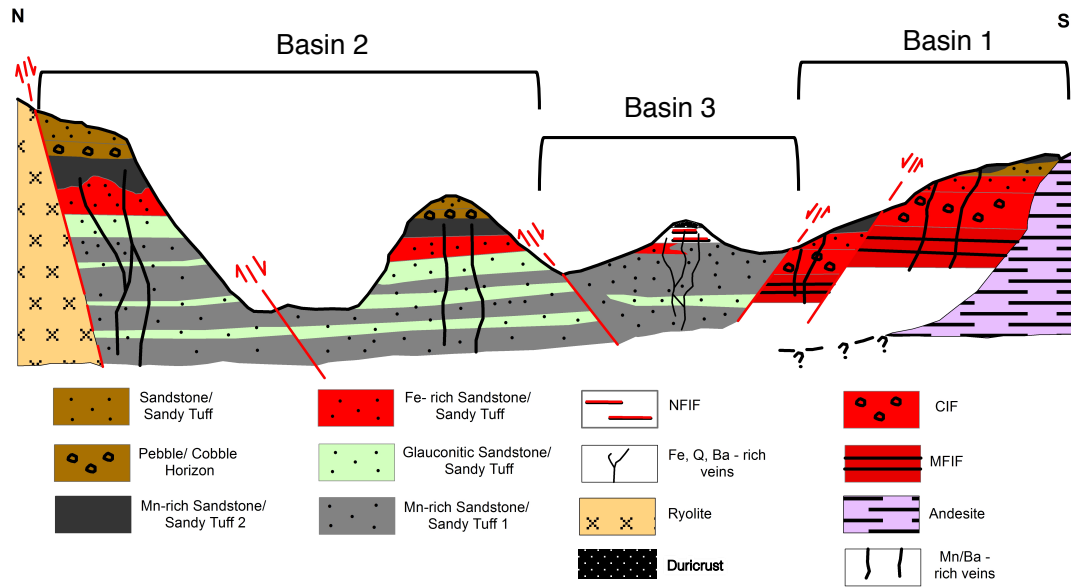


Fig. 2. Generalized schematic north-south geologic cross section through the ~1 km long CVSB showing interpreted geology, relationships between the main lithofacies, main fault locations, the iron and manganese formations, in support of a proposed three-basin hypothesis. Not drawn to scale. Four types of iron-rich sedimentary rocks occur in the CVSB. These include the iron-rich sandstones, the iron-Mn-rich sandstones, the conglomerate hosted iron formation (CIF) and the MFIF and NFIF formations that are depositionally and chemically distinct from the sandstone deposits.

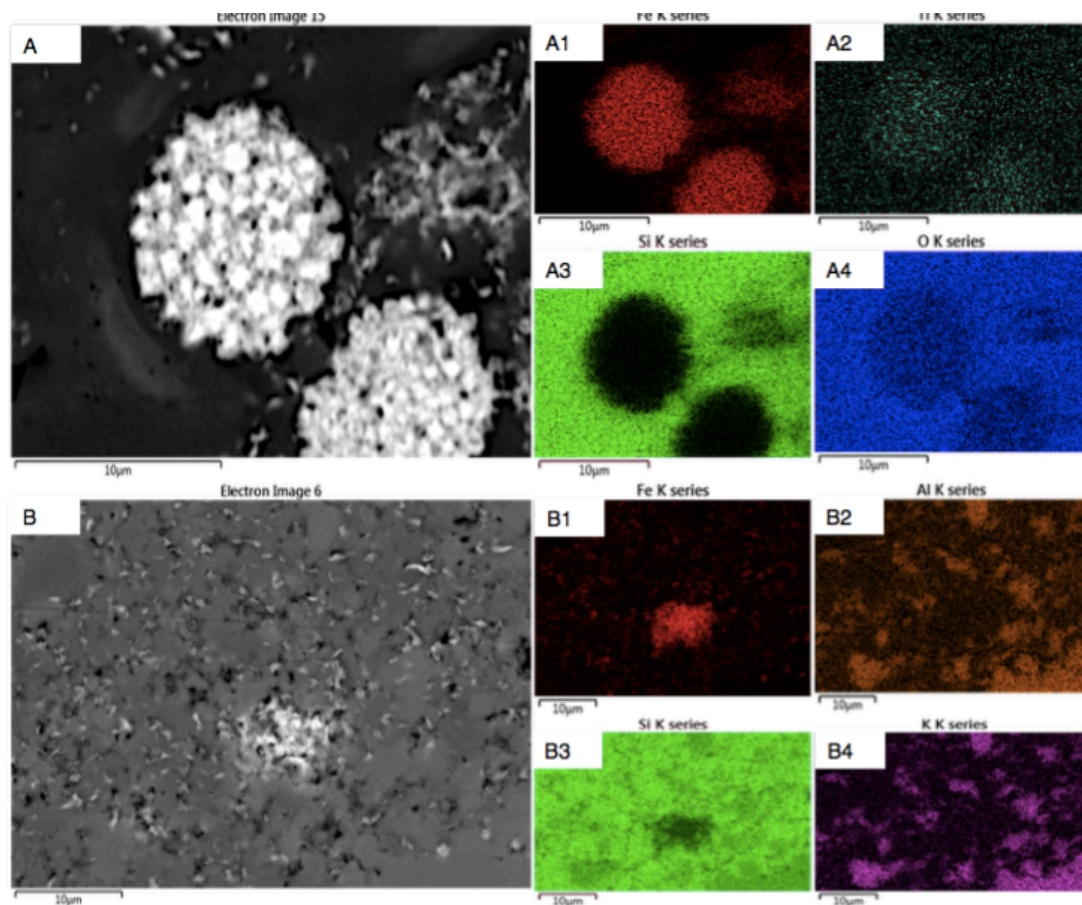


Fig. 3. EDS-electron image showing different Fe-rich mineral phases in a Si-rich matrix from the MFIF. The bright colours correspond to the analysed elements. (A), framboidal hematite particles. A1-A4, different element compositions associated with framboidal particles in panel A. (B), Dispersed fluffy Fe-rich mineral grains. B1-B4, corresponding elements associated with the micrograph in panel A.

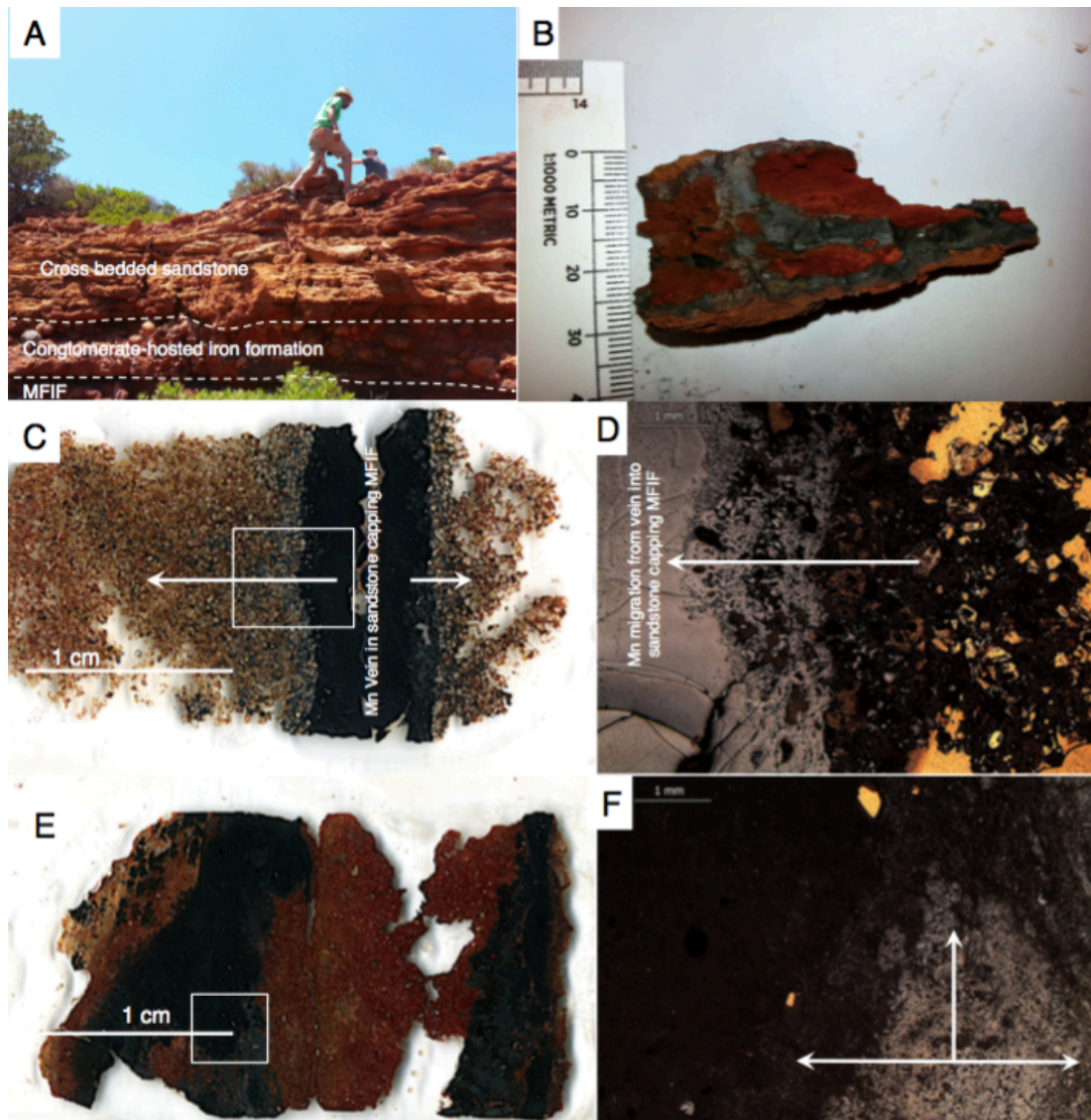
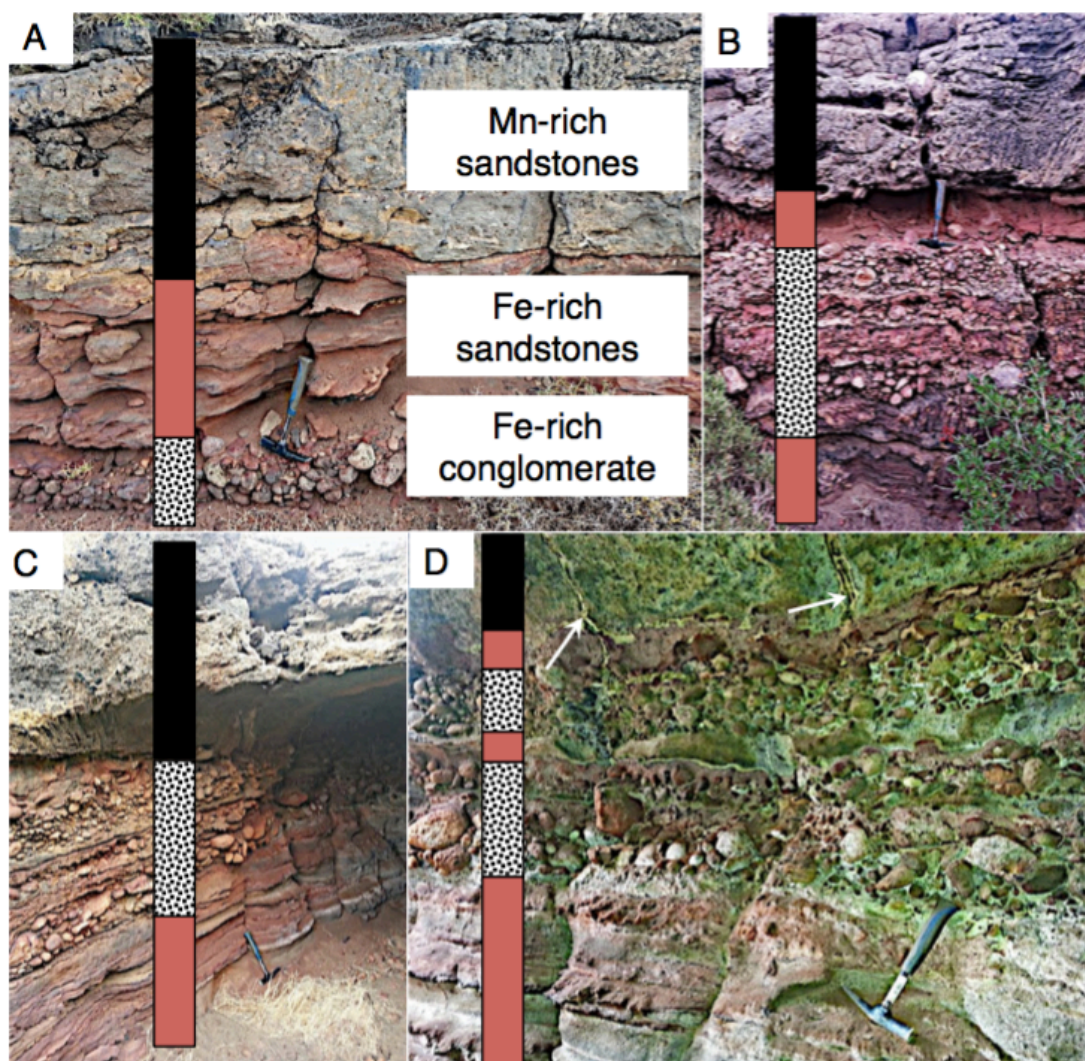


Fig. 4. Sedimentary profile, thin section scans and optical microscope images of the MFIF. (A), Field photo showing the sedimentary profile of the MFIF characterized by the overlying sandstone cap. (B), Photograph showing black diffused Mn-rich bands near the base of the MFIF. (C), Scanned image of thin section showing a black Mn-rich vein in the overlying MFIF sandstone showing a gradient of Mn migrating into the sandstone matrix (white arrows). (D), Light microscopy images showing details in panel C. (E), Scanned image of an MFIF thin section showing black Mn bands migration into a red iron-rich background. (F), Amplified light microscope image showing gray Mn layers migrating into a black Fe-rich matrix. White arrows show direction of movement. Boxes in C and E are amplified in D and F.



1468

1469 Fig. 5. Sedimentary sequence overlying the MFIF, consisting of thin (< 0.5 m)
 1470 polymictic andesite-dacite cobble-pebble, and sandstone-sandy tuff pebble, and Fe-
 1471 rich conglomerate facies overlain by thinly laminated Fe-rich sandstone beds. This
 1472 vertical sequence is interpreted to represent a progressively deeper water environment
 1473 deepening-upward sequence (A) as a result of sea level rise due to tectonic
 1474 subsidence. The multiple cycles shown in panels B-D signify several potential
 1475 episodes or sea level rise. Arrows in panel D showing hydrothermal feeder veins
 1476 feeding the overlying layers. The sequence is overlain by a thin package of parallel
 1477 and cross-bedded Mn-sandstone cap.

1478

1479

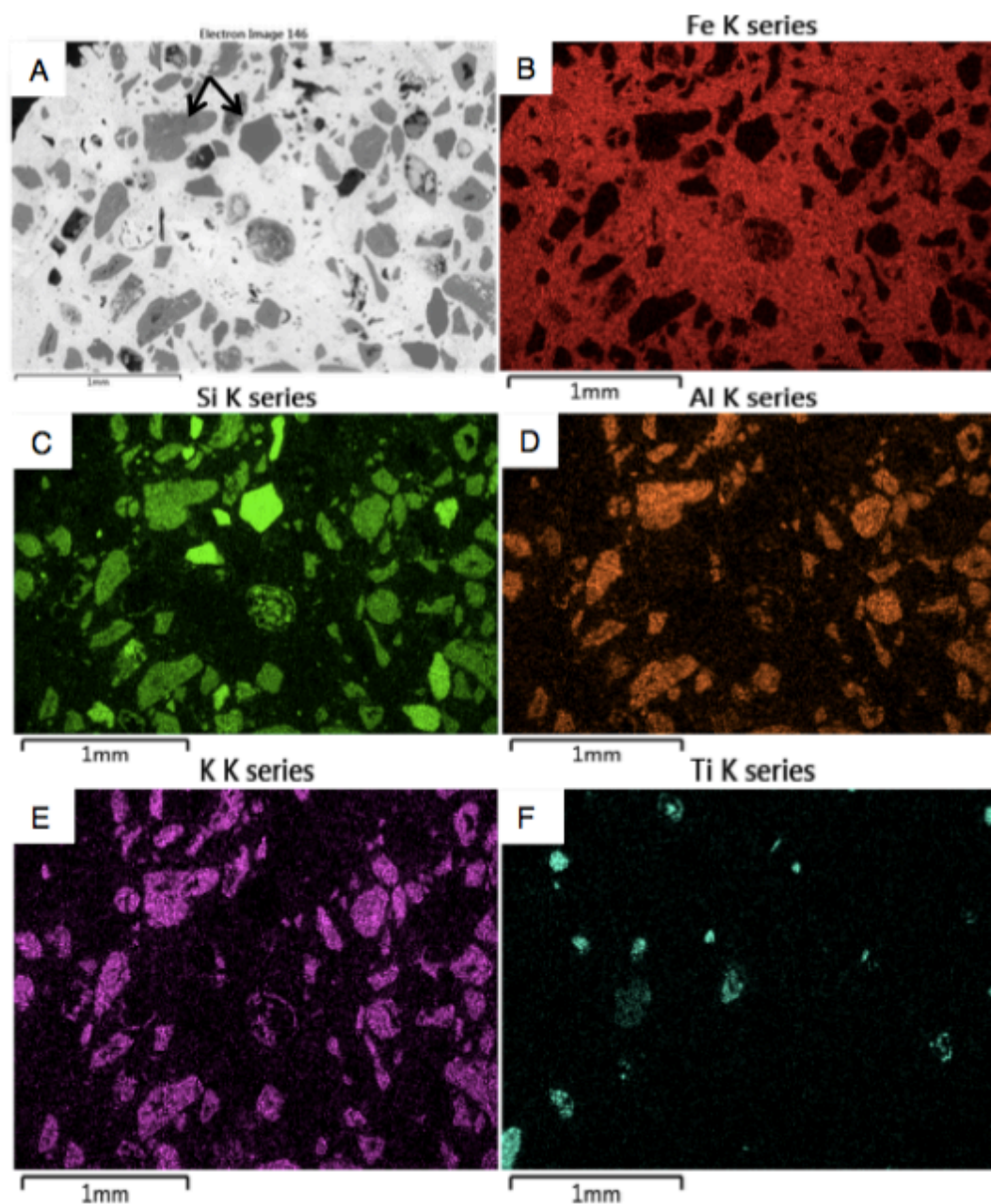
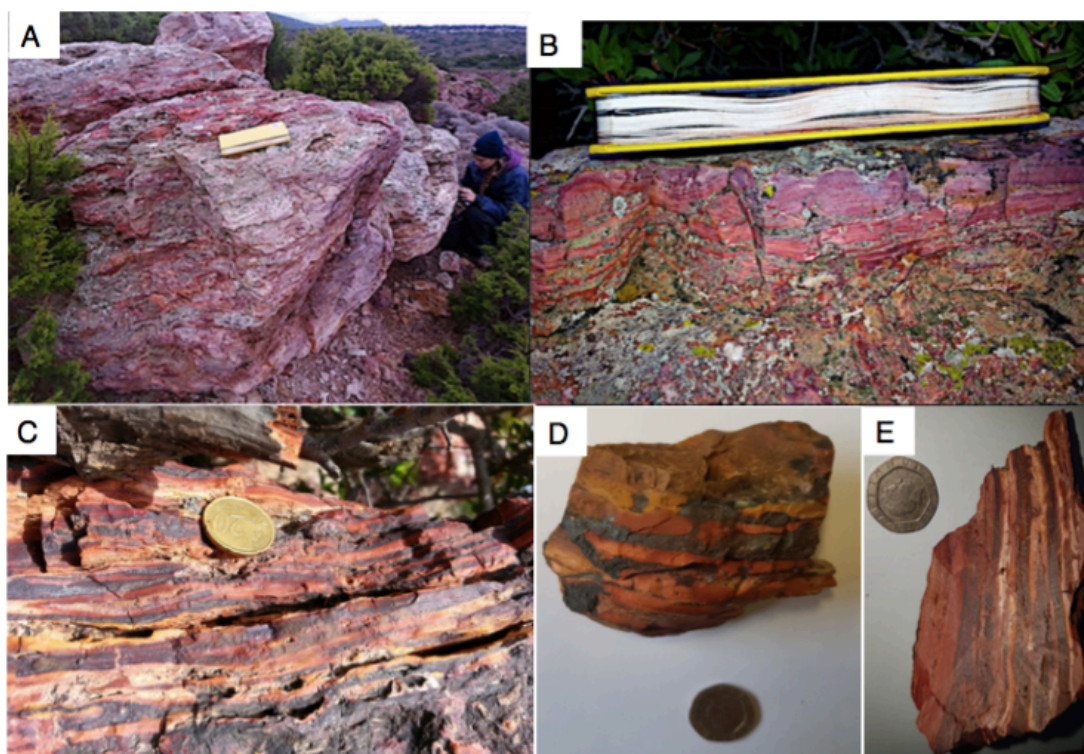


Fig. 6. Scanning electron microscope electron image of the volcaniclastic (K-feldspar)/ iron-rich sandstone conglomerate overlying the MFIF.



1485

1486 Fig. 7. Typical NFIF banded iron rocks. (A-C), Field photographs. (D), Handheld
 1487 banded Fe sample. (E), Sawn NFIF sample with laminated Fe-rich bands alternating
 1488 with Si-rich bands.
 1489

1490

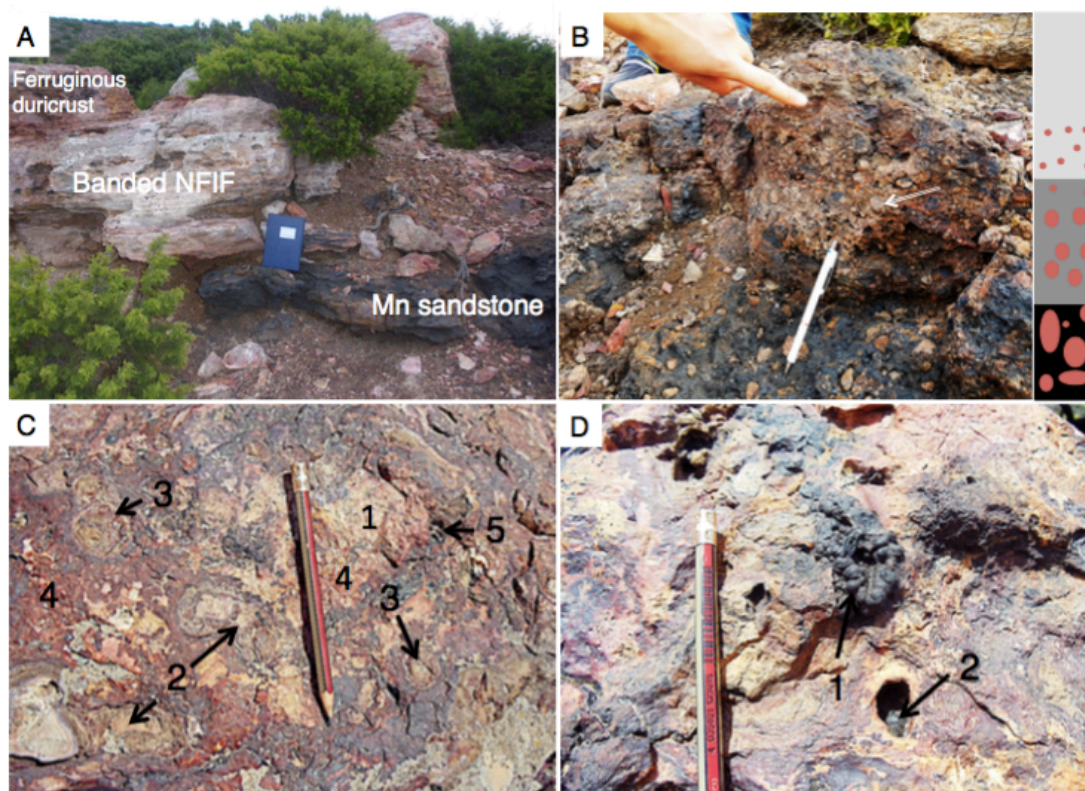


Fig. 8. Field sedimentology and stratigraphy of Section B sequence containing the NFIF. (A), Sharp boundary between lower Mn sandstone and unconformably overlying NFIF capped by a ferruginous duricrust. (B), Sandstone-sandy tuff pebble to gravel conglomerate lag facies, showing an upward fining character and bored clasts (black), locally overlies the Mn sandstone and capped by a sharp erosional contact with the overlying NFIF. The tip of the pen (7 cm long) rests on late blue-black Mn oxide overprint. (C), Ferruginous duricrust that comprises lithic fragments composed of (1) Fe-nodules (2) and Fe-concretions (3) in a hematite-rich matrix (4). (D), Matrix dissolution resulting in vermiform Mn nodules (1) and cavity black Mn oxide (2) infillings, post-dating the ferruginous duricrust formation.

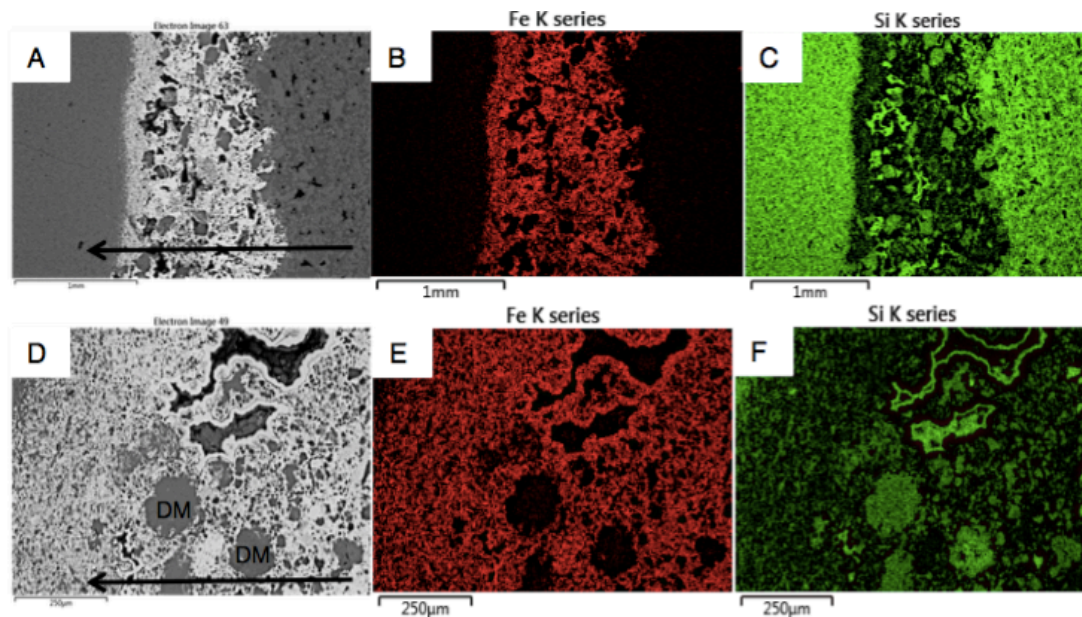


Fig. 9. EDS-electron image showing major elemental composition of typical Fe bands alternating with Si-rich layers in the NFIF. Volcaniclastic detritus mostly present in the Fe-rich bands, suggests precipitation during active submarine volcanism. To the contrary, the Si-rich bands are composed of more fine-grain, signifying deposition during periods of minimal volcanic activity. Arrows in panels (A) and (B) depict the direction of sedimentation, which was often seen to proceed from an Fe-rich matrix mixed with large grains of volcaniclastic detritus (DM) to one composed essentially of very fine-grained Fe particles before transitioning into the very fine-grained Si-rich layer. An upward fining of the volcaniclastic particles in the Fe-rich layers transitions from one made up of volcaniclastic debris and hematite, to a mainly thin hematite-rich horizon at the top of this mixed layer (see supplementary Figs 8-11 for details). This concurrent occurrence of volcaniclast and Fe oxides and the upward fining nature of the Fe-rich layers, suggest the release and oxidation of Fe(II) coincided with the settling of hydrothermal debris resulting from the introduction of enormous amount of reduced materials into the water column (Bekker et al., 2010). The iron-rich layer ceased forming as hydrothermal/volcanic release of Fe subsided, followed by deposition of the Si-rich layer. This repetitive cycle of events is observed for tens of metres laterally and vertically, stressing that the layers are not single isolated or post-depositional replacement events, but chemical precipitates that sequentially sedimented out of the water column. Red colour in Panels (B) and (C) depict Fe and green in panels (C) and (F), Si.

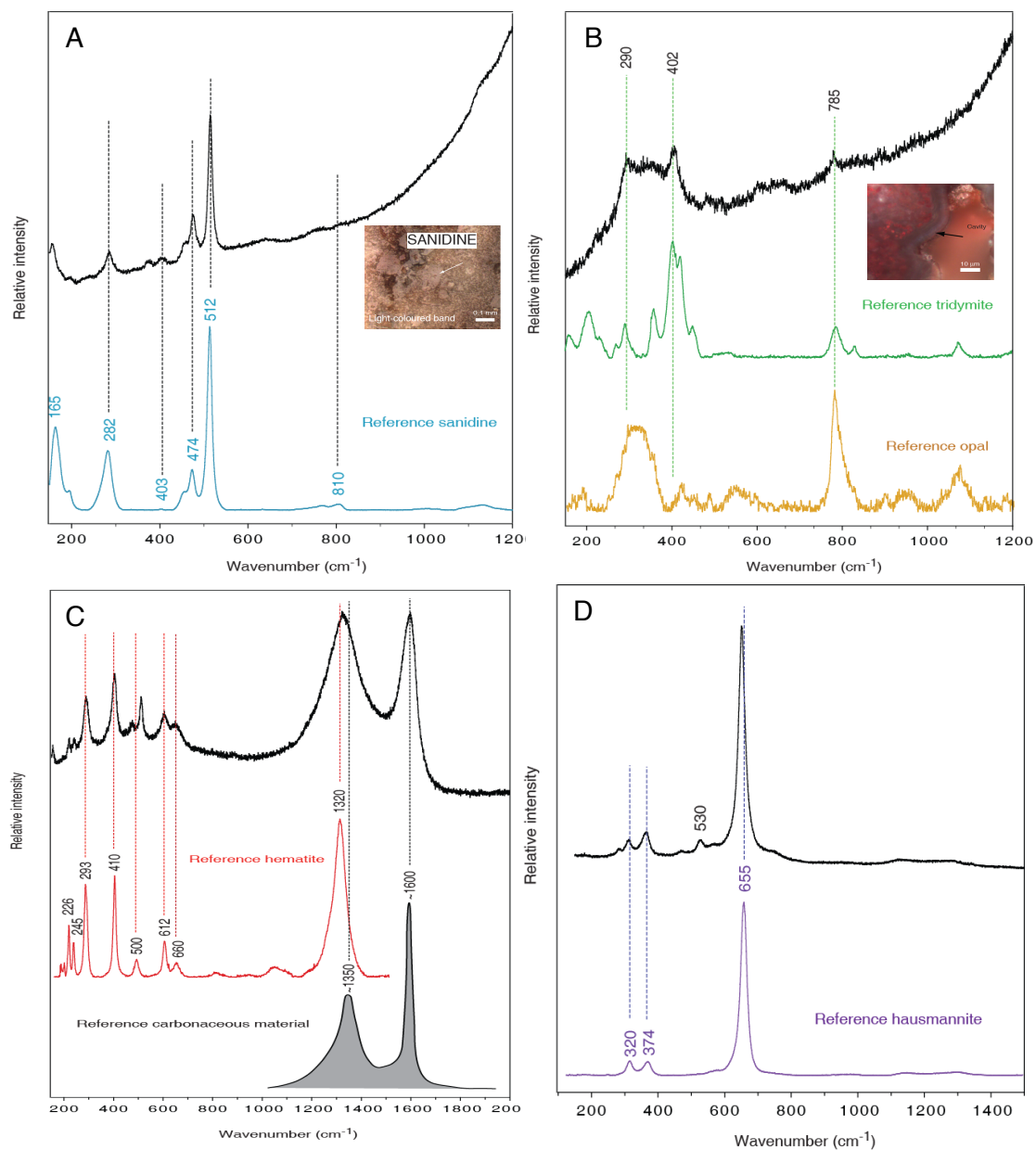
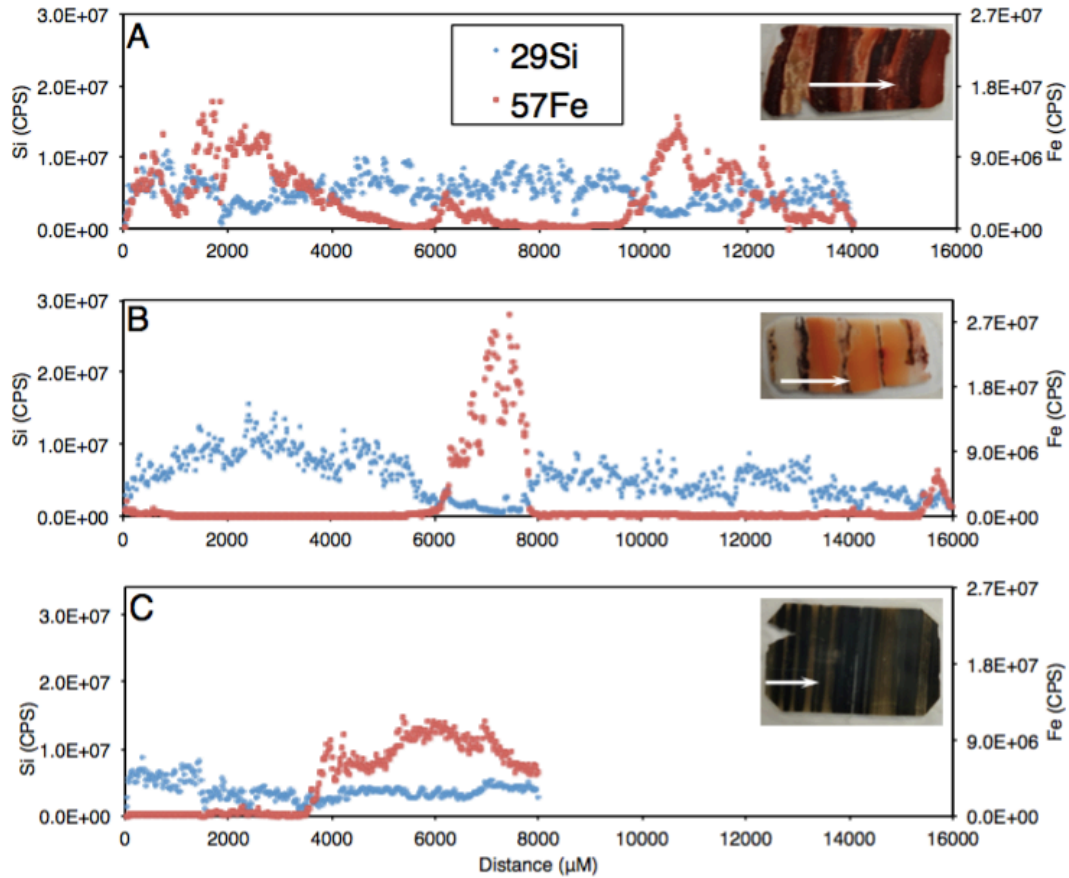


Fig. 10. Raman spectroscopy of the Fe- and/or Si-rich bands from NFIF.



1531

1532 Fig. 11. Fluctuation in Si and Fe content measured by in situ laser ablation ICP-MS
 1533 analysis. (A), Milos BIF-type rock with evenly distributed Si and iron rich bands. (B),
 1534 Milos BIF type rock with large Si bands (whitish-brownish strips) and narrow Fe-rich
 1535 bands (dark strips). (C), An example for the 2.5 Ga Kuruman BIF. Insets are analyzed
 1536 thin sections. For scale, each thin section is ≈ 3.3 cm long. White arrow on thin section
 1537 indicates analyzed area.

1538

1539

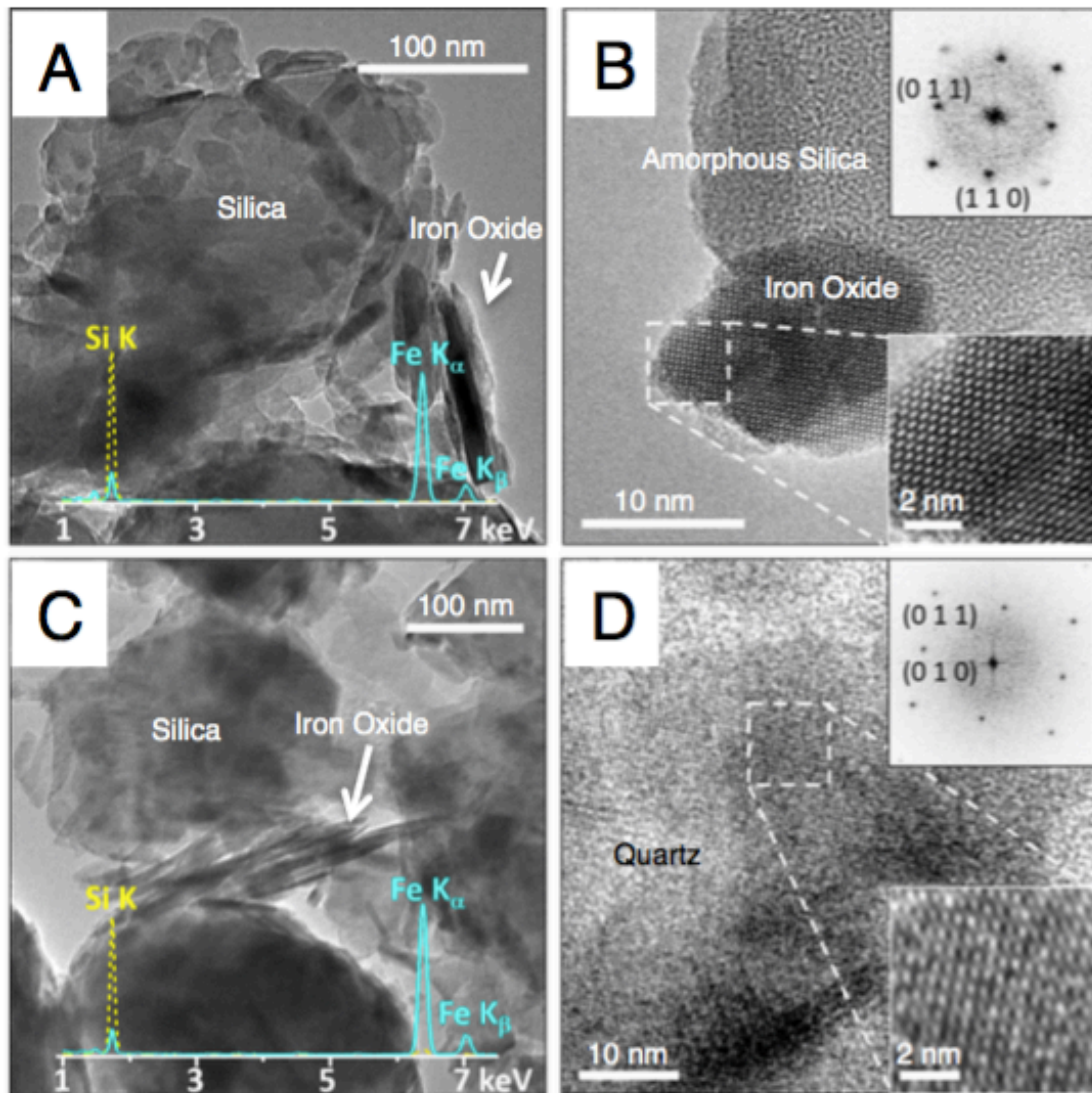


Fig. 12. TEM characterization of an NFIF and MFIF specimen. (A) lower magnification MFIF TEM-BF image. (B) High resolution images of NFIF showing amorphous Si and iron oxide crystalline lattice structures. Insets highlight a hematite particle viewed from the $[1-11]$ axis (Rhombohedral lattice). (C) Lower magnification MFIF TEM-BF image. (D) High resolution images of MFIF showing crystalline quartz and iron oxide crystalline lattice structures. Insets in (D) show a quartz crystal viewed from the $[100]$ axis. Both samples contain silica with a few hundred nm particle size, and smaller needle-like iron oxide particles. Spectral lines in panels (A) and (C) are X-ray Energy Dispersive elemental profiles of the individual Fe and Si mineral phases.

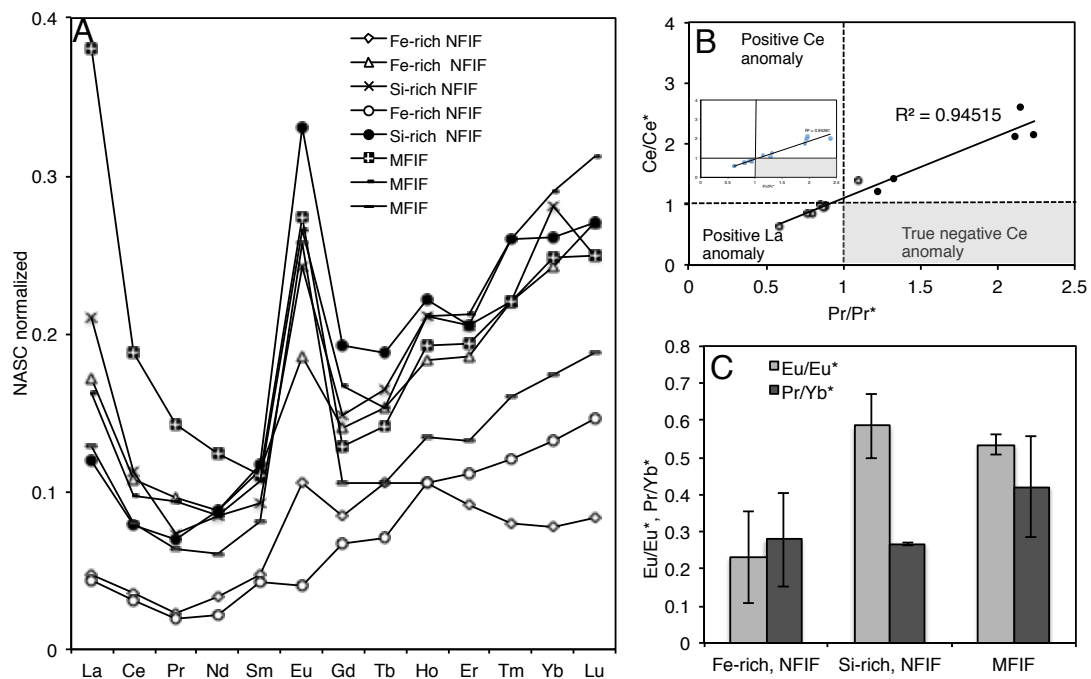
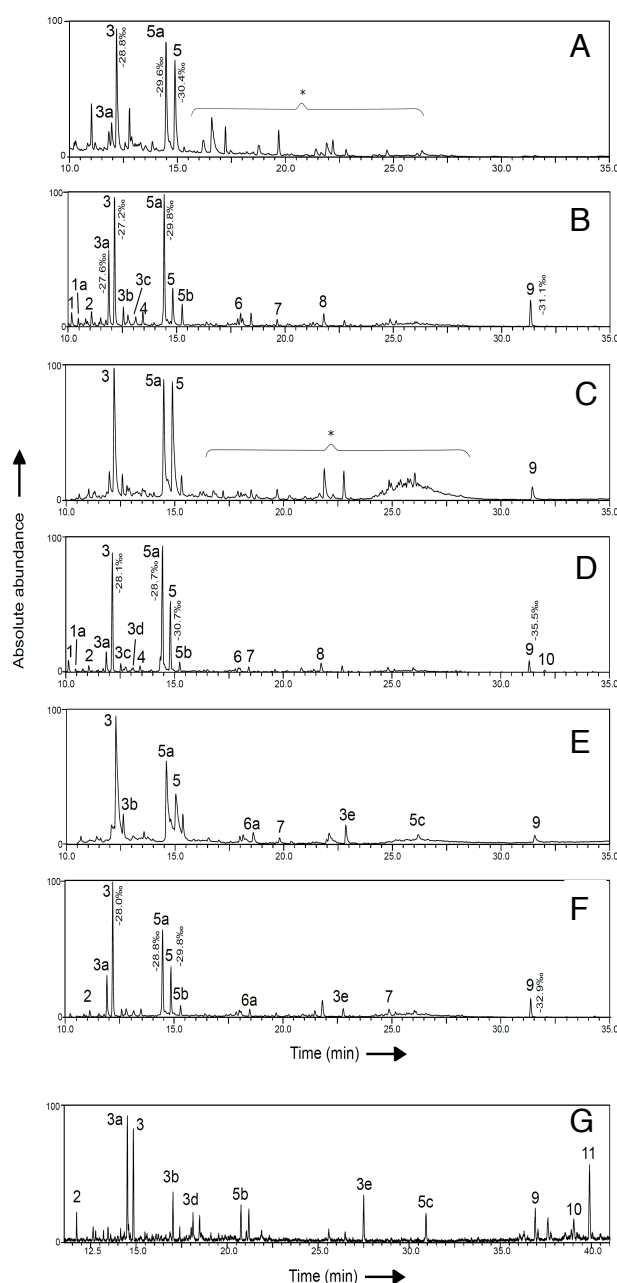


Fig. 14. Rare earth element (REE) distribution in samples and calculated Ce and Eu anomalies. (A), NASC normalized REE distribution in various rock facies. (B), Ce and Eu anomalies. (C), Eu anomalies and light REE (LREE) vs. heavy REE (HREE). Similar trends were reproduced when REE data were normalized with the Post Archean Australian Shale standard (McLennan, 1989; Bau and Dulski, 1986). This is exemplified by the insert in B.



1598

1599 Fig. 15. GC/MS chromatogram sections of total lipid extracts of the BIF (A-F) for
 1600 bands excised from the sawn rock in Figure 7E. Panel G illustrates a total lipid extract
 1601 of modern sediment from the Milos basin. Values beside peaks indicate the lipid-
 1602 specific $\delta^{13}\text{C}$ values in per mil. Because of the low intensity of the lipids recovered, it
 1603 was not possible to obtain $\delta^{13}\text{C}$ values specific for all peaks. Peaks are annotated as;
 1604 FAME = fatty acid methyl ester; Me = methyl group; TMS = trimethylsilyl; TMSE =
 1605 trimethylsilyl ester. (1) $\text{C}_{14:0}$ FAME, (1a) $\text{C}_{14:0}$ 13Me FAME, (2) $\text{C}_{15:0}$ FAME, (3)
 1606 $\text{C}_{16:0}$ FAME, (3a) $\text{C}_{16:9}$ FAME, (3b) $\text{C}_{16:0}$ TMS, (3c) 10Me $\text{C}_{16:0}$ FAME, (3d) $\text{C}_{16:9}$
 1607 FAME, (3e) $\text{C}_{16:0}$ TMSE, (4) $\text{C}_{17:0}$ TMS, (5) $\text{C}_{18:0}$ FAME, (5a) $\text{C}_{18:9}$ FAME, (5b) $\text{C}_{18:0}$
 1608 TMS, (5c) $\text{C}_{18:0}$ TMSE, (6) $\text{C}_{19:0}$ FAME, (6a) $\text{C}_{19:0}$ 18Me TMS, (7) $\text{C}_{21:0}$ TMS, (8)

1609 C_{22:0} TMS, (9) Cholesterol TMS, (10) Stigmasterol TMS, (11) beta-Sitosterol (*)
1610 contaminants (e.g., phthalates).
1611

1612

1613

1614

1615

1616

1617

1618

1619

1620

1621

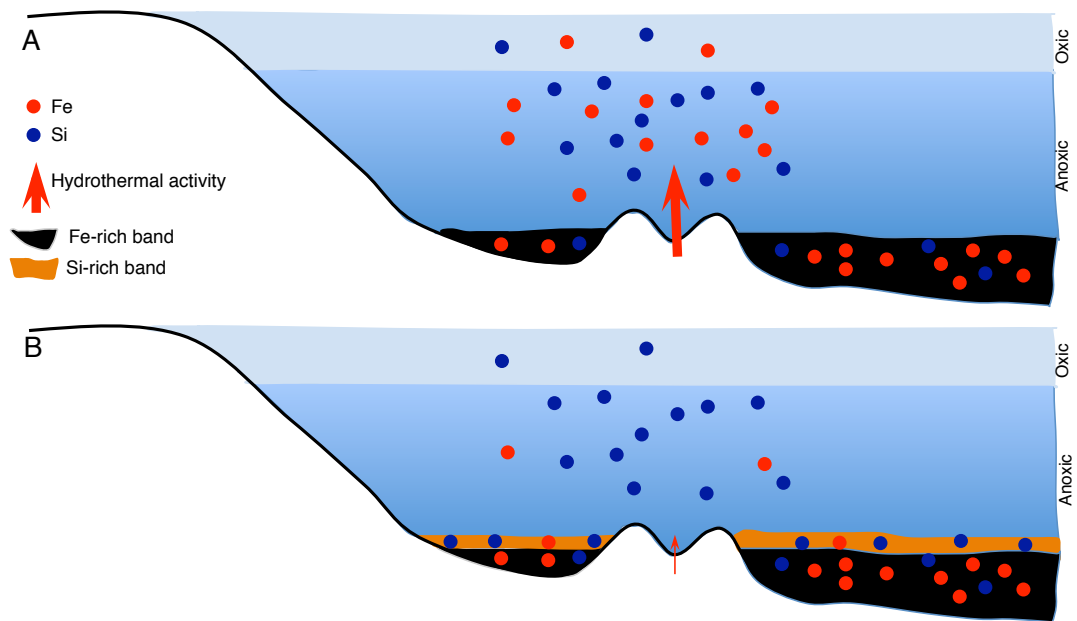
1622

1623

1624

1625

1626



1627

1628 Fig. 16. Conceptual model showing the mechanism of band formation in the NFIF
 1629 related to changes in the intensity of hydrothermal activity and chemical oxidation of
 1630 Fe(II) to Fe(III) in the water column, inferred directly from our data. See Chi Fru et
 1631 al. (2013) for a biological model for the formation of the MFIF.